

RESEARCH

Open Access



Tungsten-based polyoxometalate nanoclusters as ferroptosis inhibitors modulating S100A8/A9-mediated iron metabolism pathway for managing intracerebral haemorrhage

Yang Yang^{1,2†}, Mingzhu Lv^{1,3†}, Ruihong Liu^{1,2}, Peilu Yu^{1,2}, Ziyi Shen^{1,2}, Dazhang Bai^{1,2}, Peilin Zhao^{1,2}, Jin Yang¹, Xiaoping Tang^{1*}, Hanfeng Yang^{1*}, Yuan Yong^{1,3*} and Guohui Jiang^{1,2*}

Abstract

Background Intracerebral haemorrhage (ICH) is a devastating neurological disorder with high morbidity and mortality rates, largely owing to the lack of effective therapeutic strategies. Growing evidence has underscored the pivotal role of ferroptosis in intracerebral haemorrhage, and its contribution to neuronal death and exacerbation of brain injury, thus establishing it as a crucial target for therapeutic intervention. In recent years, polyoxometalate nanoclusters (NCs) have been applied in various neurodegenerative diseases, demonstrating neuroprotective effects. However, their impact on brain iron content and neurological function following ICH has yet to be reported. Here, we explored the potential of tungsten-based polyoxometalate (W-POM) NCs as ferroptosis inhibitors targeting the iron metabolic pathway mediated by S100A8/A9 for the treatment of ICH.

Results We successfully synthesized ultra-small reduced W-POM NCs that can rapidly cross the blood-brain barrier and are cleared through the kidney. In vitro experiments demonstrated that W-POM NCs exhibit significant and stable ROS scavenging activity while effectively alleviating iron overload and associated neuronal damage. In vivo, W-POM NCs treatment restored iron metabolism homeostasis, suppressed neuroinflammation and oxidative stress, ultimately alleviating severe neurological damage and motor deficits in ICH mice. Proteomic combined with bioinformatic analyses identified two core genes, S100A8 and S100A9, most associated with W-POM NCs intervention in ICH.

[†]Yang Yang and Mingzhu Lv contributed equally to this work.

*Correspondence:

Xiaoping Tang
nsmc_txping1971@163.com
Hanfeng Yang
yhf5@nsmc.edu.cn
Yuan Yong
yongy1816@163.com
Guohui Jiang
neurodoctor@163.com

Full list of author information is available at the end of the article



© The Author(s) 2025. **Open Access** This article is licensed under a Creative Commons Attribution-NonCommercial-NoDerivatives 4.0 International License, which permits any non-commercial use, sharing, distribution and reproduction in any medium or format, as long as you give appropriate credit to the original author(s) and the source, provide a link to the Creative Commons licence, and indicate if you modified the licensed material. You do not have permission under this licence to share adapted material derived from this article or parts of it. The images or other third party material in this article are included in the article's Creative Commons licence, unless indicated otherwise in a credit line to the material. If material is not included in the article's Creative Commons licence and your intended use is not permitted by statutory regulation or exceeds the permitted use, you will need to obtain permission directly from the copyright holder. To view a copy of this licence, visit <http://creativecommons.org/licenses/by-nc-nd/4.0/>.

Further experiments confirmed that W-POM NCs act by modulating the toll-like receptor 4/hepcidin/ferroportin signaling pathway, thereby regulating iron metabolism and reducing secondary brain injury.

Conclusions This study pioneers the application of polyoxometalates in intracerebral haemorrhage, offering a novel and promising therapeutic approach for the management of ferroptosis-related brain injuries.

Keywords Ferroptosis inhibitor, Intracerebral haemorrhage, Iron metabolism, Neuroprotection

Background

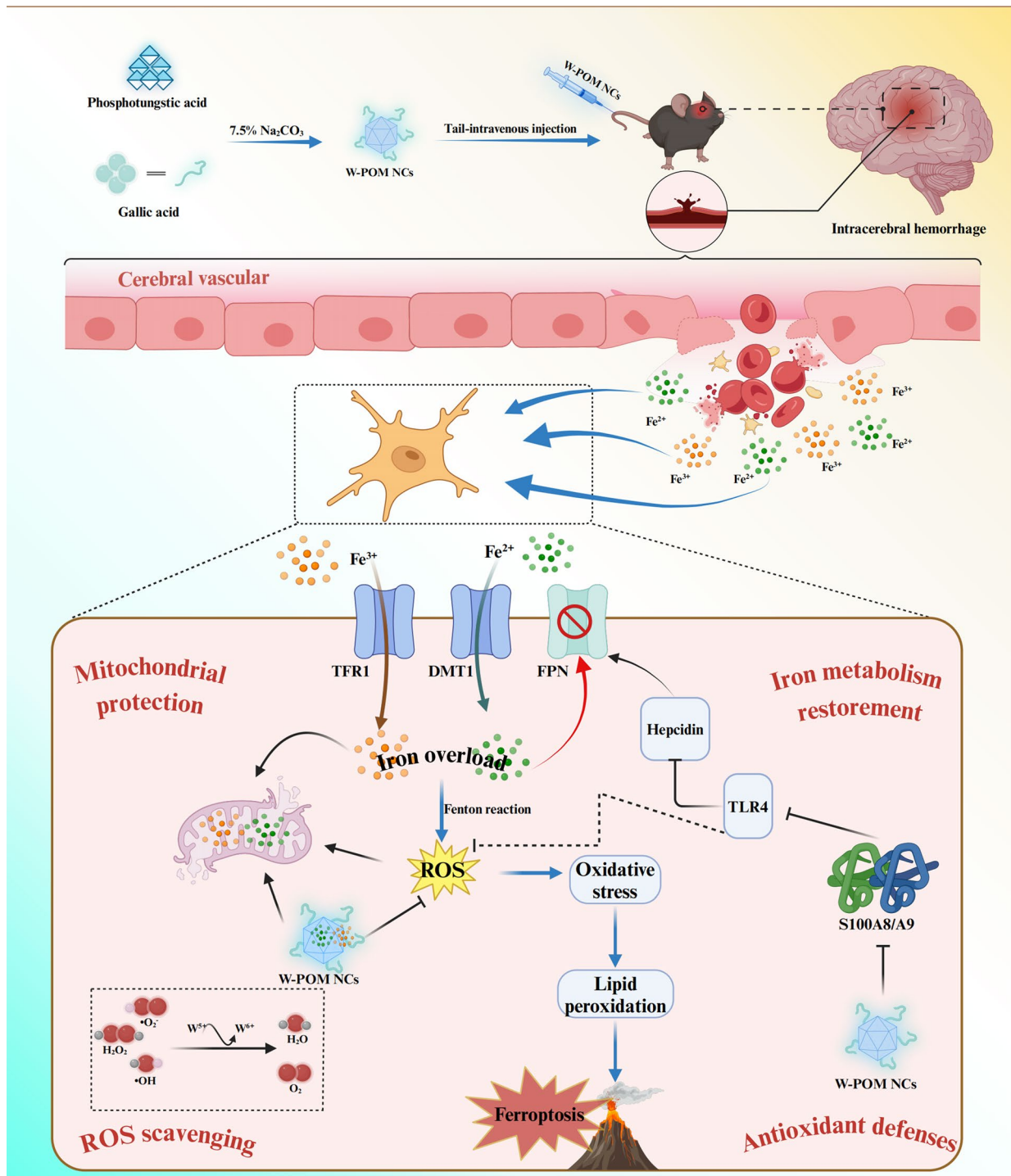
Intracerebral haemorrhage (ICH) is a severe type of stroke that is usually caused by the rupture of blood vessels within the brain, leading to bleeding into brain tissue [1]. It has a very high incidence, disability, and mortality rates [2]. Current treatments for ICH include mainly surgical interventions, haematoma evacuation, and symptomatic management [3, 4]. However, although existing treatment measures can alleviate this condition, there are still several limitations. Surgical intervention may not be suitable for some patients with ICH, particularly in cases in which the haemorrhage is deep or is located in complex areas [5]. Furthermore, after surgery and evacuation of the haemorrhage, patients often experience significant secondary brain injury, which can affect the final outcome of treatment [3]. Existing pharmacological treatments focus primarily on controlling hypertension, anti-coagulation, and improving cerebral blood flow. However, these methods often have limited efficacy and may result in certain side effects [6]. Therefore, new breakthroughs in ICH treatment strategies are needed, specifically the development of new drugs aimed at intervening in secondary injury processes after ICH through multiple pathways, with the goal of more effectively protecting the brain tissue, reducing brain damage, and improving long-term functional recovery.

The breakdown of red blood cells leads to the release of haemoglobin and its subsequent degradation into haeme and iron, contributing to a toxic environment within the brain [7]. Iron accumulation catalyses the production of reactive oxygen species (ROS), thereby intensifying lipid peroxidation. Lipid peroxides, which are highly reactive, can severely damage cell membranes and organelles, thereby initiating ferroptosis [8]. Unlike apoptosis, necrosis, and autophagy, ferroptosis is characterised by elevated intracellular iron levels and accumulation of lipid peroxides [9]. Furthermore, ferroptosis is often accompanied by suppression or depletion of cellular antioxidant systems such as glutathione and peroxisomes, which reduce the ability of cells to counter oxidative stress [10]. Given the critical role of ferroptosis in the pathology of ICH, it is crucial to investigate the underlying mechanisms and patterns of ferroptosis after ICH to develop potential therapeutic strategies.

In recent decades, nanomedicine has been widely used for the treatment of clinical diseases, including tumours,

osteoarthritis, and diabetes [11–13]. Despite their promising potential, the application of nanomedicines in central nervous system (CNS) disorders faces significant challenges. One main obstacle is the effective crossing of the blood–brain barrier (BBB), which remains a major hurdle in delivering adequate drug concentrations to the brain [14]. Furthermore, concerns have been raised regarding nanomaterial accumulation in the brain and other organs, which can lead to toxicity and adverse side effects [15]. These challenges highlight the need for continued research to optimise the safe and effective use of nanomedicines in CNS therapies. Polyoxometalates (POMs) are a class of polymers composed of transition-metal oxides. In recent years, their application in CNS diseases has gained increasing attention [16, 17]. These nanoclusters demonstrate the potential for the treatment and diagnosis of neurological disorders owing to their excellent three-dimensional structure, good biocompatibility, and unique electronic structure. Zhao et al. [18] designed and synthesised an organic platinum-substituted polyoxometalate ($\text{Pt}^{\text{II}}\text{-PW}_{11}$), which effectively inhibited $\text{A}\beta$ aggregation through interactions such as coordination bonds, electrostatic attraction, hydrogen bonds, and van der Waals forces. The $\text{Pt}^{\text{II}}\text{-PW}_{11}$ treatment prevented memory loss in amyloid precursor protein/presenilin 1 (APP/PS1) transgenic Alzheimer's disease mice. Li et al. [19] revealed that intrathecally injected POMs rapidly reached the ischaemic penumbra in a rat model of brain ischaemia–reperfusion injury and effectively scavenged ROS to inhibit oxidative stress. However, the application of POMs in the treatment of ICH remains unexplored, making it a potential area of innovation.

In this study, we successfully synthesised reduced tungsten (W)-based POM nanoclusters (W-POM NCs), which can interfere with ferroptosis-driven ICH progression through multiple pathways (Scheme 1). W-POM NCs are notably small, exhibit high safety profiles, and demonstrate an effective ability to cross the BBB. W-POM NCs with $\text{W}^{5+}/\text{W}^{6+}$ mixed valences are susceptible to changes in their valence state under certain conditions, which contributes to their significant ROS-scavenging activity. Furthermore, given that ICH is characterised by severe oxidative stress and secondary brain injury owing to iron overload, the antioxidant properties of W-POM NCs make them suitable for this condition.



Scheme 1 W-POM NCs for managing intracerebral haemorrhage. Schematic illustration of W-POM NCs inhibiting ferroptosis by modulating the S100A8/A9-mediated iron metabolism pathway. The nanoclusters targeted oxidative stress and iron dysregulation to manage ICH, demonstrating their potential for neuroprotection and therapeutic efficacy. The figures were created using BioRender.com. ICH, intracerebral haemorrhage; W-POM NCs, tungsten-based polyoxometalate nanoclusters; TFR1, Transferrin Receptor 1; DMT1, Divalent Metal Transporter 1; FPN, Ferroportin; TLR4, Toll-like receptor 4; ROS, Reactive Oxygen Species

Our innovative approach involves leveraging these properties of W-POM NCs to not only target excessive ROS and iron accumulation in the brain post-ICH but also to mitigate subsequent neuronal damage and inflammation.

Furthermore, proteomic analysis and *in vivo* studies strongly confirmed that the therapeutic mechanism of W-POM NCs in an ICH mouse model is primarily linked to S100A8/A9, a heterodimeric complex of calcium-binding proteins involved in numerous pathological processes [20]. W-POM modulates S100A8/A9, thereby regulating the expression of toll-like receptor 4 (TLR4), ferroporin (FPN), and hepcidin, which are key regulators of iron homeostasis [21]. This modulation ultimately improves post-ICH brain iron metabolism abnormalities, reduces secondary brain damage, and enhances cognitive and motor functions. This novel application could pave the way for new therapeutic strategies for ICH, potentially improving outcomes by comprehensively addressing the complex pathology of the disease.

Methods

Preparation of W-POM NCs

W-POM NCs were synthesised according to a previously reported method [22]. Gallic acid (100 mg, G131992, Aladdin, China) was dissolved in 6 mL of ultrapure water until the solution became clear and transparent. Then, 1 mL of a 60 mg/mL aqueous solution of phosphotungstic acid (P829844, Macklin, China) was added and vigorously stirred at room temperature until the solution turned orange. Subsequently, 3 mL of 7.5% sodium carbonate solution (S818014, Macklin, China) was added, and the mixture was stirred at room temperature for 5 h. Finally, the dark green W-POM NCs solution was dialysed at room temperature for 6–8 h, freeze-dried, and stored at 4 °C for further use.

Characterisation and *in vitro* evaluation of ROS-scavenging capacities

The morphology and size of the synthesised W-POM NCs were examined using transmission electron microscopy (TEM). The samples were prepared by placing a drop of the W-POM NCs suspension on a carbon-coated copper grid, followed by drying under ambient conditions. The hydrodynamic size distribution and the zeta potential of W-POM NCs were measured using dynamic light scattering (DLS) (Zetasizer Nano S90, Malvern, UK). The samples were dispersed in deionised water, and each measurement was repeated three times to ensure consistency. Fourier-transform infrared (FTIR) spectroscopy was performed to identify the functional groups present in W-POM NCs. The spectra were recorded using an FTIR spectrometer (IRTracer 100, Shimadzu, Japan) in the range of 4000–400 cm^{-1} . X-ray diffraction (XRD) analysis was conducted to determine the

crystalline structure of W-POM NCs. The XRD patterns were recorded using an X-ray diffractometer (Ultima IV, Rigaku, Japan). The crystallite size was calculated using the Debye–Scherrer equation. Energy dispersive X-ray spectroscopy (EDS) (XFlash 6130, BRUKER, GER) was used to analyse the elemental composition of W-POM NCs. The EDS analysis was performed in conjunction with TEM to confirm the presence and distribution of elements within the samples. X-ray photoelectron spectroscopy (XPS) was used to investigate the surface chemical composition and oxidation states of the elements present in W-POM NCs. XPS spectra were obtained using an XPS system (NEXSA, ThermoFisher, US) with Al K α radiation as the X-ray source. Electron spin resonance (ESR) spectroscopy was used to detect and quantify unpaired electrons in the samples to assess the generation of ROS. ESR spectra were recorded at room temperature using an ESR spectrometer (Emx-Plus, Bruker, GER) with the samples placed in quartz tubes. The optical properties and absorbance spectra of W-POM NCs were measured using an ultraviolet (UV)-Vis spectrophotometer (UV-3600 Plus, Shimadzu, Japan). Measurements were made in the range of 200 to 800 nm, with the samples dispersed in a suitable solvent. The $\bullet\text{OH}$ scavenging capacity was tested following the procedure described in the Hydroxyl Radical Assay Kit instructions (A018-1-1, Njjcbio, China), with enzyme-labelling measured at 550 nm. The $\bullet\text{O}_2^-$ scavenging capacity was evaluated using the Superoxide Anion Detection Kit (AKAO001M, Boxbio, China), with enzyme-labelling measured at 595 nm.

Cell viability assay

Cell viability was assessed using the cell counting kit (CCK)-8 (C0038, Beyotime, China), following the manufacturer's protocol. HT22 cells were seeded in 96-well plates at a density of 5×10^3 cells per well in 100 μL of Dulbecco's Modified Eagle Medium (DMEM, C11995-500B, Gibco, US) supplemented with 10% foetal bovine serum and 1% penicillin-streptomycin (v/v). After overnight incubation at 37 °C in a humidified atmosphere containing 5% CO_2 , the medium was replaced with fresh DMEM containing varying concentrations of W-POM NCs (0, 0.75, 1.5, 3.125, 6.25, 12.5, 25, and 50 $\mu\text{mol/L}$). The cells were then incubated for an additional 24 h under the same conditions. To evaluate the cytotoxicity of FAC-induced iron overload, HT22 cells were treated with different concentrations of ferric ammonium citrate (FAC, A100170, Aladdin, China) (0, 37.5, 75, 150, 300, 600, 1200 $\mu\text{mol/L}$) for 24 h. Following treatment, the medium was removed, and 100 μL of fresh medium containing 10 μL of CCK-8 solution was added to each well. The plates were incubated for 1 h at 37 °C. The absorbance was measured at 450 nm using a microplate reader.

Haemolysis assay

The haemolytic activity of W-POM NCs was evaluated using freshly collected rabbit erythrocytes. Blood (20 mL) was collected from the heart of healthy rabbits using a sterile syringe. Erythrocytes were isolated by centrifugation at $1000 \times g$ for 10 min and washed three times with sterile phosphate-buffered saline (PBS, pH 7.4). A 2% erythrocyte suspension was prepared by diluting washed erythrocytes in PBS. W-POM NCs were diluted to various concentrations (0, 0.75, 1.5, 3.125, 6.25, 12.5, 25, and 50 $\mu\text{mol/L}$) using PBS. A 200 μL aliquot of each W-POM NCs concentration was added to 800 μL of the 2% erythrocyte suspension in a microcentrifuge tube, resulting in a total volume of 1 mL. The mixture was gently mixed and incubated at $37 \text{ }^\circ\text{C} \pm 0.5 \text{ }^\circ\text{C}$ in a water bath for 3 h. Haemolysis was monitored at intervals of 15 min during the first hour and hourly thereafter for the remaining 2 h. After 3 h, the samples were centrifuged, and the absorbance was measured at 545 nm for each sample. Deionised water and PBS served as positive and negative controls, respectively.

ROS scavenging ability of W-POM NCs

The intracellular ROS levels were assessed using the ROS-sensitive fluorescent dye, 2',7'-dichlorofluorescein diacetate (DCFH-DA, D6470, Solarbio, China). HT22 cells were seeded in confocal dishes at a density of 5×10^4 cells per well and cultured overnight. The cells were co-incubated with 0.6 mM H_2O_2 for 2 h, then treated with W-POM NCs at different concentrations (0, 6.25, 12.5, 25, and 50 $\mu\text{mol/L}$) for 24 h. To evaluate the effects of FAC-induced iron overload on ROS levels in HT22 cells, the cells were treated with different concentrations of FAC (0, 150 $\mu\text{mol/L}$) and W-POM NCs (0, 50 $\mu\text{mol/L}$) for 36 h. Following treatment, the cells were incubated with 10 μM DCFH-DA in serum-free DMEM for 30 min at $37 \text{ }^\circ\text{C}$ in the dark. After washing with PBS to remove excess dye, ROS generation was observed under a laser confocal microscope. Fluorescence intensity, which corresponded to intracellular ROS levels, was captured using a green fluorescence channel.

To quantify intracellular ROS levels, flow cytometry analysis was performed using DCFH-DA staining. After treatment with W-POM NCs, HT22 cells were trypsinised, collected, and resuspended in PBS. The cells were incubated with 10 μM DCFH-DA at $37 \text{ }^\circ\text{C}$ for 30 min in the dark. Following incubation, the cells were washed twice with PBS and analysed using a flow cytometer with excitation at 488 nm and emission at 525 nm. The mean fluorescence intensity of DCF was used to quantify ROS levels in each sample.

To further assess ROS-mediated cytotoxicity, a live/dead cell staining assay was performed using calcein-AM and propidium iodide (PI) dual staining (CA1630;

Solarbio, China). Following ROS induction by H_2O_2 and subsequent W-POM NCs treatment, the cells were washed with PBS and incubated with 2 μM calcein-AM and 4 μM PI for 30 min at $37 \text{ }^\circ\text{C}$ in the dark. Live cells were identified by green fluorescence (calcein-AM), whereas dead cells were marked by red fluorescence (PI). Images were captured using a laser confocal microscope with the appropriate filter sets.

Mitochondrial ROS levels were assessed using the mitochondrial superoxide indicator Mito-SOX Red (M36008, Invitrogen, US). The cells were treated with different concentrations of FAC (0, 150 $\mu\text{mol/L}$) and W-POM NCs (0, 50 $\mu\text{mol/L}$) for 36 h. Following treatment, the cells were incubated with 5 μM Mito-SOX Red in serum-free DMEM at $37 \text{ }^\circ\text{C}$ for 10 min in the dark. After incubation, the cells were washed twice with PBS to remove excess dye. Mitochondrial ROS levels were visualised using a laser confocal microscopy, with excitation at 510 nm and emission at 580 nm. Images were captured in the red fluorescence channel to determine mitochondrial superoxide levels.

Iron content detection

In the *in vitro* study, approximately 1×10^6 HT22 cells were collected after treatment with 150 $\mu\text{mol/L}$ FAC, and the experiment was conducted according to the protocols of the Cell Total Iron Colorimetric Assay Kit (E-BC-K880-M, Elabscience, China) and the Cell Ferrous Iron Colorimetric Assay Kit (E-BC-K881-M, Elabscience, China). For the *in vivo* study, fresh brain tissue ($n=5$) was extracted, thoroughly homogenised, and centrifuged at $16,000 \times g$ for 10 min to remove insoluble materials. The supernatant was collected, and the iron content was measured and calculated according to the protocol of the Iron Assay Kit (MAK025, Sigma, GER).

JC-1 staining assay

To evaluate mitochondrial membrane potential (MMP) in HT22 cells, JC-1 staining (C2006, Beyotime, China) was performed according to the manufacturer's instructions. Cells were treated with varying concentrations of W-POM NCs (0, 50 $\mu\text{mol/L}$) and FAC (0, 150 $\mu\text{mol/L}$) for 36 h. After treatment, the culture medium was removed, and the cells were washed twice with PBS. The cells were then incubated with the JC-1 staining solution at $37 \text{ }^\circ\text{C}$ for 30 min in the dark. After incubation, the staining solution was removed, and the cells were washed with PBS to remove excess dye. Fluorescence was observed under a laser confocal microscope, using appropriate filter sets to detect red and green fluorescence. Images were captured, and the ratio of red to green fluorescence was analysed using image processing software to quantify changes in MMP.

Animals

Eight-week-old C57BL/6 mice, weighing 20–24 g, were purchased from Jiangsu Wukong Biotechnology Co. All animal experiments were approved by the Welfare and Ethics Review Committee of Animal Experiments at the North Sichuan Medical College (Nanchong, China) [approval No. NSMC(A)2024(053)].

The animals were housed in a pathogen-free environment with a controlled temperature of 22 ± 2 °C, a 12-h light/dark cycle, and provided with ad libitum access to food and water. The mice were randomly assigned to the following experimental groups: sham, ICH (ICH model mice), and W-POM treatment (ICH model mice treated with W-POM NCs). ICH was induced in mice as described previously [23]. Briefly, ICH was induced by injecting collagenase IV (BS165; Biosharp, China) into the right striatum. The Sham group underwent the same surgical procedure without collagenase injection. The W-POM group received W-POM NCs administered via intravenous injection in the tail 3 h after induction of ICH. Subsequently, W-POM NCs were injected into the tail vein every 24 h for 3 consecutive days. The animals were euthanised 3 days post-ICH induction for further analysis, including histological and biochemical assessments.

Behavioural tests

To assess neurological deficits following ICH, a 28-point scale for neurological disability scores (NDS) was utilised [24]. Higher scores indicated more severe neurological impairment. Mice were assessed 1- and 3-days post-ICH induction ($n = 12$). The tests were performed by a blinded investigator to minimise bias.

The open field test (OFT) was conducted to evaluate the general locomotor activity in mice. The open-field apparatus consisted of a square arena with high walls to prevent escape. The floor of the arena was divided into equal squares. Each mouse was placed in the centre of the arena, and its behaviour was recorded for 5 min using an overhead camera connected to an automated tracking system ($n = 12$).

Fluorine-18 Fluorodeoxyglucose (18FDG) micro-positron emission tomography/computed tomography (PET/CT) imaging

Mice were fasted for at least 12 h before imaging to reduce background glucose levels and enhance the contrast of the imaging results ($n = 6$). The animals were anaesthetised with isoflurane to minimise movement and stress during the imaging procedure. Anaesthesia was maintained throughout the imaging sessions to ensure consistent conditions. 18 F-FDG was administered via intravenous injection in the tail. Micro-PET/CT imaging was performed using a dedicated small animal PET/

CT scanner. CT was used for anatomical localisation and attenuation correction, whereas PET was used to acquire functional imaging data. After injecting the radiotracer, the animals were positioned in the imaging system to ensure proper alignment and minimal movement. Post-processing of PET images included attenuation correction, image co-registration, and normalisation. Regions of interest (ROIs) were defined based on anatomical landmarks from the CT images, and a quantitative analysis was performed to assess 18 F-FDG uptake. Standardised uptake values (SUVs) were calculated to quantify metabolic activity in the tissues of interest.

Brain water content assay

After the experimental intervention or treatment, the animals were euthanised according to ethical guidelines ($n = 6$). The brains were promptly removed and rinsed with cold PBS to remove blood or debris. Stereoscopic injections of the side tissue from each brain were then collected. The dissected brain tissue was immediately weighed to determine the wet weight. To ensure accurate measurements, the tissue samples were carefully blotted with filter paper to remove excess surface moisture. The wet tissue samples were then placed in an oven set at 100 °C for 24 h to ensure complete drying. After drying, the samples were cooled in a desiccator to room temperature and weighed to obtain the dry weight.

Western blotting

Brain tissue ($n = 3$) was homogenised in ice-cold RIPA buffer supplemented with protease and phosphatase inhibitors. The homogenates were then centrifuged at 12,000 $\times g$ for 15 min at 4 °C to remove insoluble materials. The protein concentration in the supernatant was determined using a BCA protein assay kit (AR1189, Boster, China) according to the manufacturer's instructions. For western blotting (WB), equal amounts of protein (30 μg per lane) were separated via sodium dodecyl sulphate-polyacrylamide gel electrophoresis (SDS-PAGE) using 10% or 15% polyacrylamide gels, depending on the molecular weight of the target proteins. Electrophoresis was performed at 120 V until the dye front reached the bottom of the gel. The proteins were transferred from the gel onto a polyvinylidene fluoride membrane using a wet transfer apparatus. The membranes were blocked with 5% non-fat dry milk in tris-buffered saline with 0.1% Tween-20 (TBST) for 1 h at room temperature to prevent non-specific antibody binding. The membranes were incubated with primary antibodies specific to the target proteins, overnight at 4 °C. The following primary antibodies were detected via WB: rabbit anti-transferrin receptor 1 (TFR1) polyclonal antibody (1:1000, AF5343, Affbiotech, China), rabbit anti-FPN polyclonal antibody (1:1000, NBP1-21502, Novus, US), rabbit anti-divalent

metal transporter 1 (DMT1) polyclonal antibody (1:1000, 20507-1-AP, Proteintech, US), rabbit anti-S100A8/A9 monoclonal antibody (1:1000, ab288715, Abcam, UK), rabbit anti-hepcidin monoclonal antibody (1:200, ab190775, Abcam, UK), anti-TLR4 polyclonal antibody (1:1000, AF7017, Affbiotech, China). Secondary antibodies (BA1054, Boster, China), conjugated with horseradish peroxidase, were applied for 1 h at room temperature. After washing with TBST, the protein bands were visualised using an enhanced chemiluminescence detection reagent and captured using a digital imaging system.

Evaluation of neuronal damage

After the experimental procedures, the animals ($n=3$) were deeply anaesthetised and transcardially perfused with cold PBS followed by 4% paraformaldehyde (PFA) diluted in PBS. Brains were carefully removed and post-fixed in 4% PFA for 24 h at 4 °C. The fixed brains were then dehydrated through a graded series of ethanol concentrations (70%, 80%, 90%, 95%, and 100%) and cleared in xylene. After dehydration, the brains were embedded in paraffin wax. Paraffin-embedded brains were sectioned at 3 μm thickness using a rotary microtome. The sections were allowed to float in a warm water bath to remove wrinkles and mounted on gelatine-coated slides. The slides were dried overnight in an oven at 37 °C to ensure proper adhesion of the sections to them.

Slides with paraffin sections were deparaffinised in xylene (two washes for 10 min each) and rehydrated through a series of decreasing ethanol concentrations (100%, 95%, and 70%), followed by rinsing with distilled water. The sections were then stained with Nissl staining solution (C0117, Beyotime, China) for 5–10 min. After staining, the sections were rinsed with distilled water and differentiated in 95% ethanol and acetic acid for a few seconds until the desired contrast was achieved. Finally, the sections were dehydrated through a graded series of ethanol concentrations, cleared in xylene, and covered with coverslips. Stained sections were examined under a bright-field microscope. Neuronal cell bodies were identified based on their characteristic dark-stained Nissl bodies.

Tissue preparation, sectioning, deparaffinisation, and rehydration were performed as described for Nissl staining. The sections were stained with Fluoro-Jade B solution (TR-150-FJB; Biosensis, AUS) for 20 min in the dark. After staining, the sections were rinsed three times with distilled water, air-dried, and covered with coverslips. FJB-positive cells, indicative of degenerating neurons, were visualised using laser confocal microscopy.

Enzyme-linked immunosorbent assay (ELISA)

Tissue homogenates ($n=5$) were collected according to standard protocols. Commercial ELISA kits specific

for the target, such as malondialdehyde (MDA, S0131S, Beyotime, China), interleukin (IL)-1 β (IL-1 β , E-EL-M0037, Elabscience, China), IL-6 (IL-6, E-EL-M0044, Elabscience, China), and tumour necrosis factor- α (TNF- α , E-EL-M3063, Elabscience, China), were used. The assay was performed according to the manufacturer's instructions.

Immunofluorescent staining

Tissue preparation ($n=3$), sectioning, deparaffinisation, and rehydration were prepared as follows. The sections were incubated in tris-EDTA antigen repair solution (C1037, Solarbio, China) at 95 °C for 20 min. After cooling to room temperature, sections were rinsed with PBS. The sections were incubated in normal goat serum (SL038, Solarbio, China) for 1 h at room temperature to reduce non-specific antibody binding. The sections were then incubated with primary antibodies specific to target antigens, overnight at 4 °C. The following primary antibodies were used: rabbit anti-Iba1 polyclonal antibody (1:500, GB113502, Servicebio, China) and rabbit anti-glial fibrillary acidic protein (GFAP) polyclonal antibody (1:200, CL488-16825, Proteintech, China). Secondary antibodies conjugated with fluorophores were applied for 1 h at room temperature in the dark. Images were captured using a confocal laser microscope.

Transmission electron microscopy

Perihaematoma brain tissues were carefully dissected and cut into small blocks (approximately 1 mm³) for optimal fixation. The tissue blocks were immersed in the same fixative solution (2.5% glutaraldehyde and 2% paraformaldehyde) for an additional 3 h at 4 °C to ensure thorough fixation. The samples were then rinsed in 0.1 M phosphate buffer (pH 7.4) for 10 min each. For enhanced contrast, the tissues were post-fixed in 1% osmium tetroxide in 0.1 M phosphate buffer for 1–2 h at 4 °C. After fixation, the samples were rinsed with distilled water three times for 10 min each. The tissue samples were dehydrated through a graded series of ethanol concentrations (30%, 50%, 70%, 90%, 95% and 100%) at 4 °C, with each step lasting 10–15 min. After ethanol dehydration, the samples were treated with propylene oxide (100%) for 10 min to prepare them for embedding. The dehydrated samples were infiltrated with a mixture of propylene oxide and epoxy resin (1:1) for 1 h, followed by overnight incubation with pure epoxy resin at room temperature. The samples were then embedded in fresh epoxy resin and polymerised at 60 °C for 24–48 h. Ultrathin sections (approximately 70 nm) were cut from embedded samples using an ultramicrotome and collected on a copper grid. The sections were stained with uranyl acetate for 10 min, followed by lead citrate for 5 min to enhance contrast. The stained sections were

examined using an HT7700 transmission electron microscope (Hitachi, Tokyo, Japan).

4D-label-free proteomic assay

The frozen tissue samples were homogenised in lysis buffer using a tissue homogeniser. The lysates were centrifuged at 14,000 $\times g$ for 20 min at 4 °C to remove debris, and the supernatants containing the proteins were collected. Protein concentrations were determined using a BCA protein assay kit (AR1189, Boster, China), according to the manufacturer's instructions. Protein digestion with trypsin was performed according to filter-aided sample preparation, described by Matthias Mann. The digest peptides of each sample were desalted on C18 Cartridges (Empore™ SPE Cartridges C18 (standard density), bed I.D. 7 mm, volume 3 mL, Sigma, GER), concentrated by vacuum centrifugation and reconstituted in 40 μ L of 0.1% (v/v) formic acid. Next, 20 μ g of protein from each sample were mixed with 5 \times loading buffer and boiled for 5 min. Proteins were separated on 12.5% SDS-PAGE gel (constant current: 14 mA, 90 min). Protein bands were visualised by Coomassie Blue R-250 staining. Liquid chromatography–tandem mass spectrometry (MS)/MS analysis was performed using a timsTOF Pro mass spectrometer (Bruker) coupled to Nanoelute (Bruker Daltonics) for 120 min. The peptides were loaded onto a reverse phase trap column (Thermo Scientific Acclaim Pep-Map100, 100 μ m \times 2 cm, nanoViper C18) connected to the C18-reversed phase analytical column (ThermoScientific Easy Column, 10 cm long, 75 μ m inner diameter, 3 μ m resin) in buffer A (0.1% formic acid) and separated with a linear gradient of buffer B (84% acetonitrile and 0.1% formic acid) at a flow rate of 300 nL/min controlled by IntelliFlow technology. The mass spectrometer was operated in the positive ion mode. The mass spectrometer collected ion mobility MS spectra over a mass range of m/z 100–1700 and 1/k0 of 0.6 to 1.6, and then performed 10 cycles of parallel accumulation serial fragmentation MS/MS with a target intensity of 1.5k and a threshold of 2500. Active exclusion was enabled at a release time of 0.4 min. The identified proteins were subjected to bioinformatics analysis, including functional annotation, pathway enrichment (e.g. KEGG, GO), and protein-protein interaction analysis (e.g. STRING).

Virus injection

S100A8/A9 overexpressing adeno-associated virus (AAV) and control AAV were customised and purchased from Aiji Biotechnology Co., Ltd. (Guangzhou, China) and named AAV-S100A8/A9 and AAV-NC, respectively. For experimental validation, C57BL/6 mice were randomly injected with AAV-S100A8/A9 or AAV-NC. After complete anaesthesia with 1% pentobarbital, the brains of the mice were fixed using a stereotaxic

apparatus. The fur on top of the head was removed and the skin was cut with ophthalmic scissors to expose the skull. A cranial drill was used to drill into the bone cavities. A Hamilton microsyringe (1 μ L) was used to inject 1 μ L of the virus into the right striatum area at a speed of 0.1 μ L/min. After each injection, the needle was left in place for 10 min, and then slowly and evenly withdrawn. After completing the viral injection, the mice were fed for another 4 weeks until viral transfection reached its peak for subsequent experiments. The expression of enhanced green fluorescent protein (EGFP) in AAV-S100A8/A9 and AAV-NC cells was used as a marker for successful viral transfection.

Statistical analysis

All experimental data were processed using SPSS statistical software and visualisations were generated using GraphPad Prism 9.5. Results are expressed as mean \pm standard error of the mean. Group differences were evaluated using a one-way analysis of variance followed by Tukey's post-hoc test for multiple comparisons. Statistical significance was defined as P value < 0.05 (*), P value < 0.01 (**), and P value < 0.001 (***) ; ns represents no statistical significance.

Results

Characterisation and ROS-scavenging activity of W-POM NCs

W-POM NCs were successfully synthesised according to previously reported strategies (Scheme 1). TEM images showed that W-POM NCs had uniform particle sizes, were evenly dispersed and did not aggregate (Fig. 1A). The diameter of the W-POM NCs was approximately 1.52 ± 0.43 nm (Additional file 1A). W-POM NCs were dispersed in deionised water, and their hydrodynamic sizes were analysed using DLS. The results showed that their hydrodynamic size was approximately 6.66 ± 0.01 nm (Additional file 1B). The hydrodynamic size of the W-POM NC was small, which may allow them to effectively cross the BBB after intravenous administration [25, 26]. The zeta potential of W-POM NCs was determined to be -22.3 mV (Additional file 1C). The negatively charged W-POM NCs exhibited greater suspension stability, which may reduce non-specific binding with proteins and other molecules in biological fluids and may improve targeting to specific tissues. As shown in Fig. 1B, we measured the UV absorption spectra of W-POM NCs at different concentrations. The absorption peak was located at approximately 631 nm, and the absorbance was positively correlated with the concentration of the W-POM NCs. In the FTIR spectrum (Fig. 1C), the characteristic absorption of W-POM at 1060.6 cm^{-1} and that of phosphotungstic acid at 1082.5 cm^{-1} were owing to the stretching vibration of the P-Oa bond. The

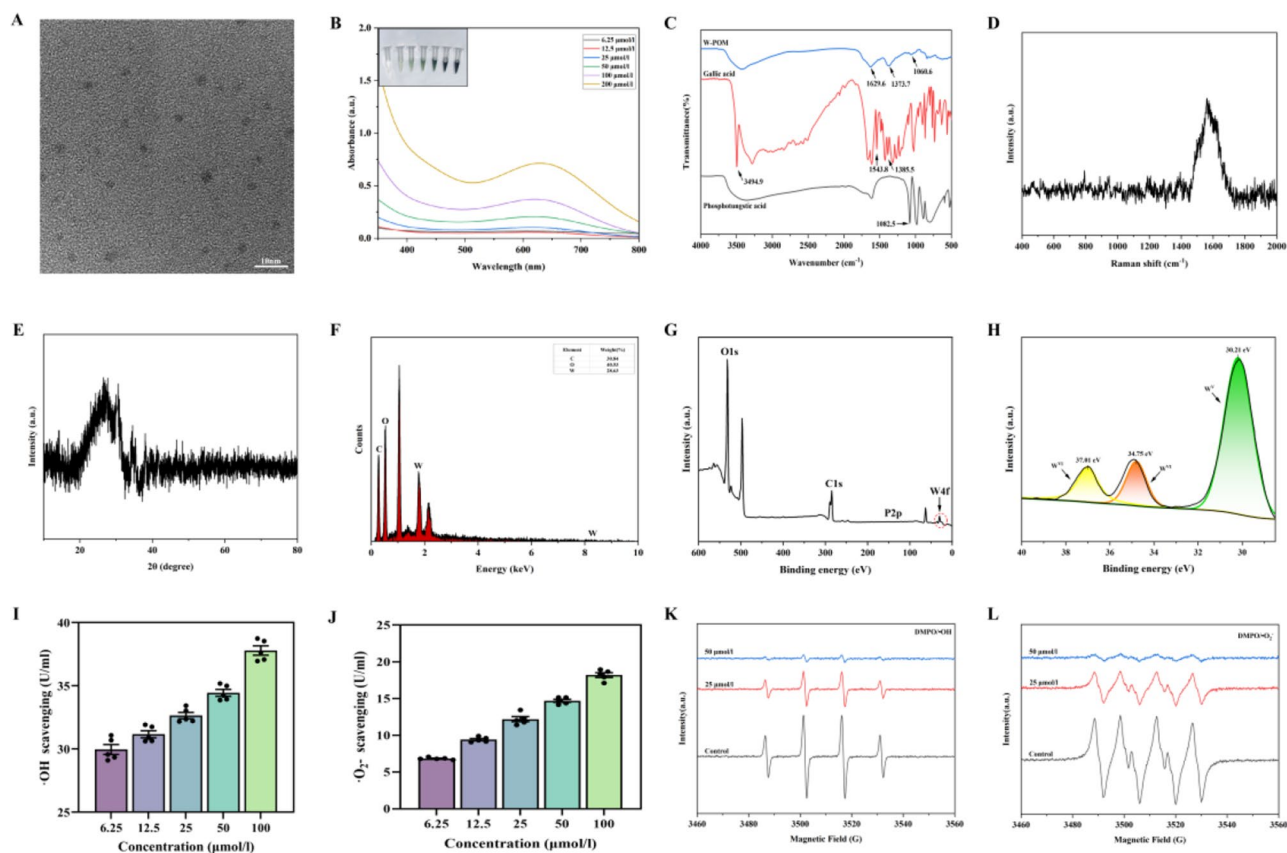


Fig. 1 Characterisation and ROS-scavenging activities of W-POM NCs. **(a)** TEM image of W-POM NCs. **(b)** UV absorption spectra of W-POM NCs at different concentrations. **(c)** FTIR spectra of W-POM NCs, phosphotungstic acid and gallic acid. **(d)** Raman spectra. **(e)** XRD pattern. **(f)** EDS spectra. **(g)** XPS full survey spectrum. **(h)** W_{4f} XPS spectra. **(i)** $\cdot OH$, **(j)** $\cdot O_2^-$ scavenging activities of W-POM NCs with enzyme-labelling measuring instrument. **(k)** $\cdot OH$, **(l)** $\cdot O_2^-$ scavenging activities of W-POM NCs illustrated by ESR spectroscopy, respectively. EDS, energy dispersive spectroscopy; ESR, electron spin resonance; FTIR, Fourier transform infrared; ICH, intracerebral haemorrhage; ROS, reactive oxygen species; TEM, transmission electron microscopy; UV, ultraviolet; W-POM NCs, tungsten-based polyoxometalate nanoclusters; XPS, X-ray photoelectron spectroscopy; XRD, X-ray diffraction; $\cdot O_2^-$, superoxide radicals; $\cdot OH$, hydroxyl radicals

symmetric and asymmetric stretching vibrations of the carboxyl group resulted in characteristic absorptions at 1629.6 cm^{-1} and 1373.7 cm^{-1} , respectively. The successful fabrication of W-POM NCs was further confirmed through Raman spectroscopy and powder XRD (Fig. 1D, E). EDS revealed that Carbon (C), Oxygen (O), and Tungsten (W) were uniformly distributed in W-POM NCs, with C accounting for approximately 30.84%, O for approximately 40.53%, and W for approximately 28.63% of the space (Fig. 1F). XPS further confirmed the presence of chemical elements (O, C, P, and W) in W-POM NCs (Fig. 1G). High-resolution XPS spectra of W_{4f} indicated the presence of mixed valence states (W^{5+}/W^{6+}) in W-POM NCs (Fig. 1H), suggesting that W-POM NCs exhibit good reduction properties. In summary, these characterisations indicated that W-POM NCs were successfully constructed and may serve as a promising nanomedicine with a considerable potential for biomedical applications.

In addition, this study used ROS (superoxide radicals $\cdot O_2^-$, hydroxyl radicals $\cdot OH$) to evaluate the ROS scavenging activity of W-POM NCs at different concentrations. After the addition of W-POM NCs, $\cdot O_2^-$ and $\cdot OH$ were consumed, and their characteristic absorption peaks decreased, indicating that W-POM NCs could effectively scavenge excess ROS (Fig. 1I, J). According to electron spin resonance (ESR) spectroscopy, W-POM NCs effectively neutralised $\cdot OH$ (Fig. 1K) and $\cdot O_2^-$ (Fig. 1L), demonstrating a dose-dependent scavenging capability. Overall, W-POM NCs can effectively reduce excess ROS and exhibit excellent free radical scavenging performance.

Cell-killing and ROS-scavenging by W-POM in HT22 cell

Previous studies have demonstrated the low cytotoxicity of POMs [22, 27–29], which is consistent with our CCK-8 assay results (Fig. 2A), indicating that W-POM NCs had minimal cell-killing effects. After incubation with $50\text{ }\mu\text{mol/L}$ of W-POM NCs for 24 h, the CCK-8

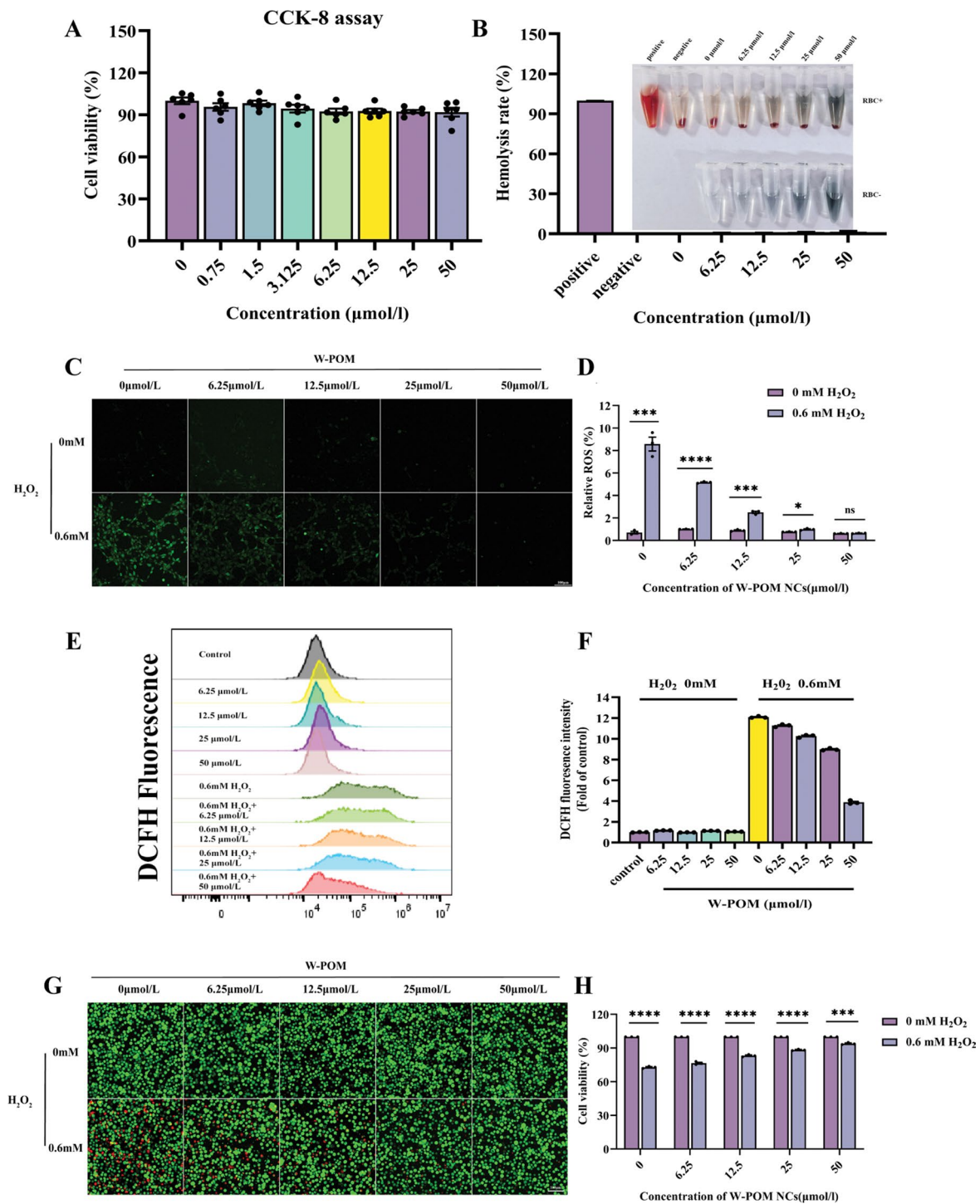


Fig. 2 Characterisation of cell killing capacity of W-POM NCs and scavenging of ROS in HT22 cell. **(a)** CCK-8 assays performed after incubation with gradient concentration of W-POM NCs. **(b)** Haemolysis assay. **(c)** Representative images of ROS staining with DCFH-DA in HT22 cells subjected to different treatments and the corresponding quantitative analysis of ROS levels **(d)**. (scale bar, 100 µm) **(e)** Flow cytometry analysis with DCFH-DA staining and **(f)** the corresponding mean fluorescence intensity. **(g)** Representative images from the typical live/dead cell staining assay in HT22 cells subjected to different treatments and **(h)** the corresponding quantitative analysis of cell survival rate. (scale bar, 100 µm). (**P* < 0.05, ***P* < 0.01, ****P* < 0.001, means ± SEM). CCK, cell counting kit; ROS, reactive oxygen species; W-POM NCs, tungsten-based polyoxometalate nanoclusters

assay revealed that the survival percentage of HT22 cells remained at $91.88 \pm 7.7\%$. With an increase in the concentration of W-POM NCs, no significant decrease in the survival rate of HT22 cells was observed. The results of the haemolysis test indicated that W-POM NCs exhibited low haemolytic activity (haemolysis rates were below 4%), further demonstrating their good biocompatibility (Fig. 2B).

Next, we evaluated the protective effects of W-POM NCs on HT22 cells under H_2O_2 -induced oxidative stress. Under stimulation of 0.6 mM H_2O_2 , a large amount of ROS was produced in the cells. A DCFH-DA fluorescent probe was used to detect ROS levels. Non-fluorescent DCFH-DA reacts within cells to generate DCF, which emits green fluorescence, allowing the observation of ROS content [30, 31]. After HT22 cells were co-cultured with 0.6 mM H_2O_2 for 2 h, W-POM NCs were added and incubated for another 24 h. As the concentration of W-POM NCs increased, the intensity of green fluorescence gradually decreased (Fig. 2C, D, Additional file 2), strongly demonstrating that W-POM NCs effectively scavenged intracellular ROS. Furthermore, we quantified ROS levels in HT22 cells using flow cytometry. As shown in Fig. 2E and F, the relative fluorescence intensity in cells without H_2O_2 treatment was < 1.5 . In contrast, after the addition of H_2O_2 , the relative fluorescence intensity increased sharply to 12.09 ± 0.08 . The relative fluorescence intensity gradually decreased with increasing concentrations of W-POM NCs. When 50 $\mu\text{mol/L}$ of W-POM NCs was added, the relative fluorescence intensity decreased to 3.88 ± 0.16 . These observations indicate that W-POM NCs can effectively scavenge intracellular ROS and that the scavenging rate is positively correlated with the concentration.

We used calcein-AM/PI co-staining HT22 cells to label live and dead HT22 cells, respectively. As shown in Fig. 2G and H, the W-POM NCs protected HT22 cells from H_2O_2 -induced oxidative stress by scavenging ROS. Therefore, all these findings suggest that W-POM NCs, with their low cytotoxicity, have a good potential for scavenging ROS.

Anti-ferroptosis properties of W-POM in FAC-induced iron overload HT22 cells

Oxidative stress occurs owing to activation of the Fenton reaction by excess intracellular iron ions, causing damage to mitochondrial morphology and function [32–34]. Based on previously reported methods [35], we used FAC to induce an iron-overloaded cell model in HT22 cells, to further validate the efficacy of W-POM NCs in inhibiting ferroptosis *in vitro*. The CCK8 assay (Additional file 3) revealed that the viability of HT22 cells decreased as the FAC concentration increased. We ultimately selected a 150 $\mu\text{mol/L}$ FAC concentration to induce the iron

overload cell model (cell viability = $54.58 \pm 5.72\%$). FAC stimulation significantly increased iron levels in HT22 cells, confirming the successful establishment of an iron-overloaded neuronal model (Fig. 3A, B). Total and ferrous iron levels within the cells in the FAC group were significantly higher than those in the cells in the control group (which did not receive FAC or W-POM). After W-POM intervention, the iron content in the FAC group was significantly reduced. Subsequently, we measured the ROS content in each group of cells using DCFH-DA fluorescence staining (Fig. 3C, D). Compared with the control group, the FAC stimulation group exhibited significantly elevated ROS levels; in contrast, the ROS levels in the cells treated with W-POM partially recovered.

Mitochondria play a critical role in ferroptosis as the primary site of iron accumulation and ROS generation, which drive lipid peroxidation and ultimately lead to cell death [36]. Mito-SOX Red is a fluorogenic dye that specifically targets mitochondria. As shown in Fig. 3E and F, W-POM treatment exhibited a satisfactory effect in inhibiting mitochondrial ROS production. These results strongly demonstrated that W-POM can target mitochondria, effectively eliminating ROS and counteracting oxidative stress caused by iron deposition. JC-1 is a dual fluorescent dye that forms aggregates within mitochondria and emits red fluorescence at a high membrane potential. Conversely, at low membrane potentials, it remains in a monomeric form and emits green fluorescence. JC-1 staining showed that FAC stimulation significantly inhibited red fluorescence and promoted green fluorescence (Fig. 3G–I). However, after W-POM NCs treatment, red fluorescent JC-1 aggregates were significantly restored. TEM images revealed that after FAC stimulation, the mitochondrial membrane ruptured, and the number of mitochondrial cristae markedly reduced, to the point of complete disappearance (Fig. 3J). These results indicated that W-POM NCs improved oxidative stress and mitochondrial dysfunction induced by iron overload.

Neurological impairment and brain oedema ameliorated by W-POM in the ICH mouse model

We established a mouse model of ICH using collagenase IV to investigate the therapeutic effects of W-POM NCs. We randomly divided C57/BL6 mice into the following three groups: sham group (C57/BL6 mice without collagenase injection), ICH group (ICH mouse model), and W-POM group (ICH mice treated with W-POM NCs). Based on previous studies [22], we conducted preliminary experiments using different concentrations of W-POM NCs (20, 40, and 80 mg/kg). As shown in Fig. 4A, W-POM NCs were administered via intravenous injection in the tail 3 h after successfully creating an ICH mouse model. Intravenous administration was continued

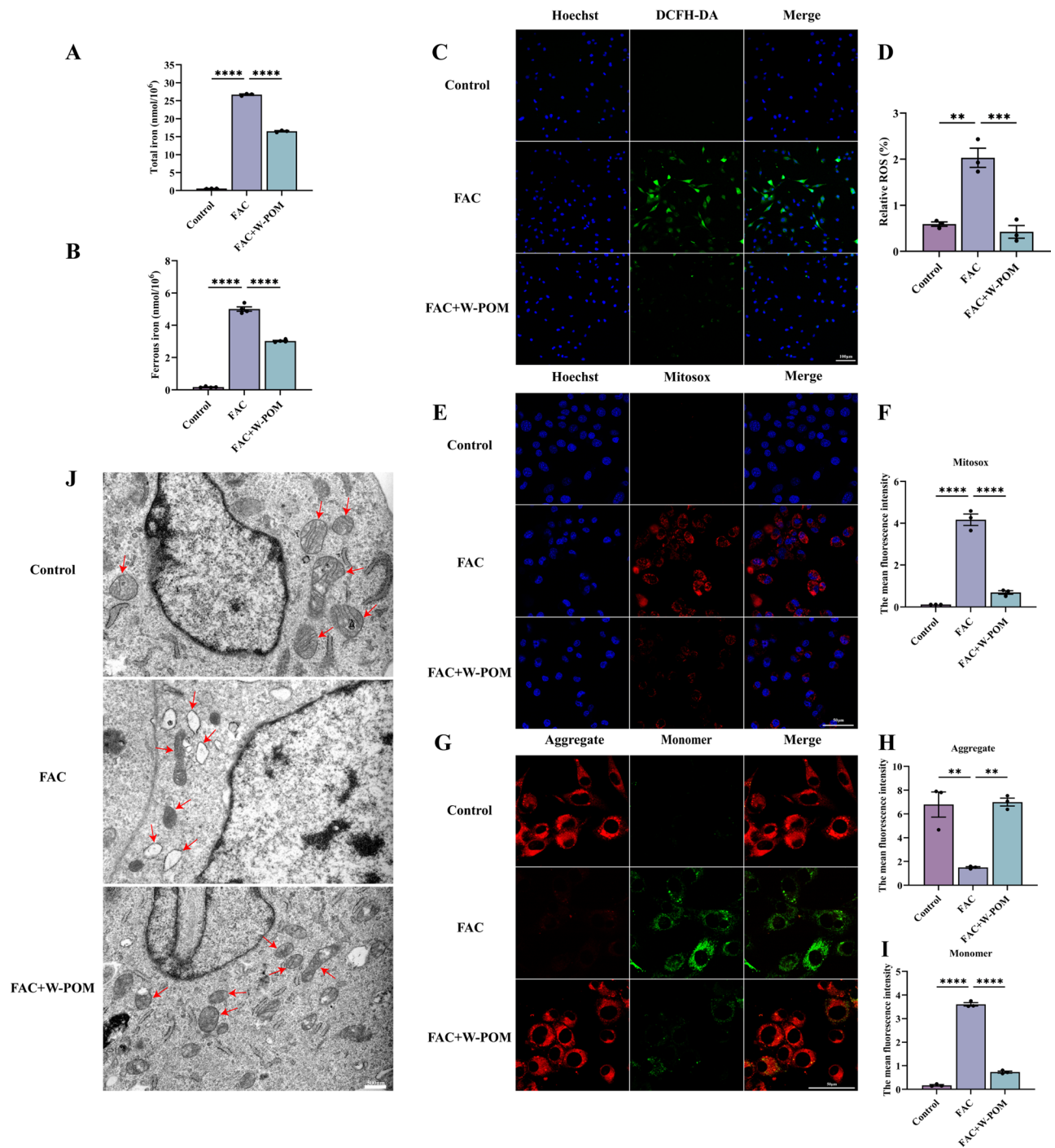


Fig. 3 W-POM NCs exert neuroprotective effects by inhibiting iron overload-induced oxidative stress and mitochondrial dysfunction. (a,b) Iron content detection in HT22 cells after various treatments. (c) Representative images of DCFH-DA staining and (d) quantitative analysis. (scale bar, 100 μ m). (e) Representative confocal fluorescence images of Mito-SOX staining and (f) quantitative analysis. (scale bar, 50 μ m). (g) Representative images of JC-1 staining and (h,i) quantitative analysis. Red, JC-1 aggregates; green, JC-1 monomers. (scale bar, 50 μ m) (j) Representative TEM images of mitochondrial morphology in HT22 cells after various treatments. Red arrows indicate mitochondria. (scale bar, 500 nm). (* P < 0.05, ** P < 0.01, *** P < 0.001, means \pm SEM). TEM, transmission electron microscopy; W-POM NCs, tungsten-based polyoxometalate nanoclusters

for 3 consecutive days and behavioural tests were performed at 24 and 72 h. First, NDS [24] was obtained for the ICH mice. A higher NDS score indicated more severe neurological impairment. As shown in Fig. 4B and C,

the NDS scores were lower for the of the W-POM group than for the ICH group 24 and 72 h after ICH, indicating that W-POM NCs treatment alleviated neurological deficits in ICH mice. For subsequent evaluation of

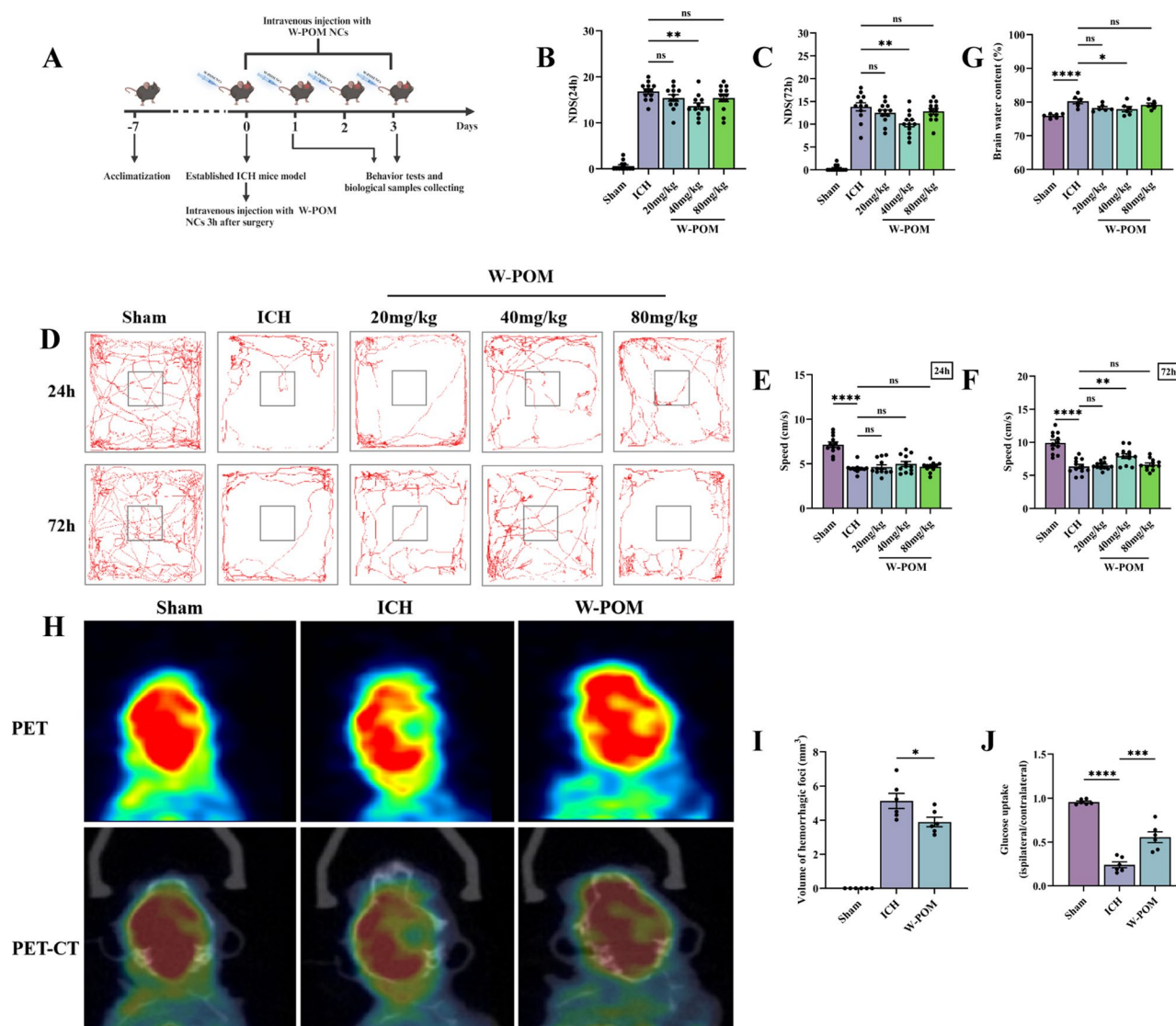


Fig. 4 W-POM NCS alleviate ICH-induced neurologic impairment, haematoma volume, and brain oedema after ICH. (a) Schematic illustrating the treatment schedule for ICH mice. Figure created with BioRender.com. NDS at 24 h (b) and 72 h (c) after intravenous injection with various doses of W-POM NCS. (d) Representative motion trajectories of the open field test. Average velocity during the open field test at 24 h (e) and 72 h (f) after intravenous injection with various dose of W-POM NCS. (g) Brain water content of the ipsilateral brain tissue at 72 h after surgery in ICH mice model. (h) PET-CT images of ICH mice model (coronal sections). The shadow represents the haemorrhagic focus. Quantitative analysis of the volume of the haemorrhagic focus (i) and glucose uptake in the peripheral area of the haemorrhagic foci (j) assessed on PET-CT scan. (* $P < 0.05$, ** $P < 0.01$, *** $P < 0.001$, means \pm SEM). CT, computed tomography; ICH, intracerebral haemorrhage; NDS, neurological disability score; PET, positron emission tomography; TEM, transmission electron microscopy; W-POM NCS, tungsten-based polyoxometalate nanoclusters

motor behaviour, we first conducted an OFT to assess the movement ability of the mice (Fig. 4D-F). Compared to untreated ICH mice, those treated with W-POM NCS exhibited a better average speed during the treatment period, with a significant difference observed 72 h after ICH (Fig. 4F). This indicated that W-POM NCS significantly alleviated motor dysfunction in ICH mice. Furthermore, we assessed the degree of brain oedema by measuring the water content in the brain tissue on the haemorrhagic lesion side (Fig. 4G), which when compared with the sham group, had increased significantly

72 h after ICH. On the contrary, the W-POM group showed reduced brain water content on the haemorrhagic lesion side, with the most significant reduction observed in the 40 mg/kg W-POM NCS treatment group. Based on the comparison of the therapeutic effects of different concentrations of W-POM NCS, we selected 40 mg/kg for subsequent in vivo experiments.

After ICH, haematoma formation exerts mechanical pressure on the surrounding neurons, causing direct damage. We used ^{18}F -FDG micro-PET/CT to observe the location, morphology, and size of the haematoma

in ICH mice model and to explore the metabolic activity at the haemorrhagic lesion site [37, 38]. As shown in Fig. 4H, ^{18}F -FDG was uniformly distributed in the mice brain in the sham group, whereas in the ICH group, ^{18}F -FDG uptake was reduced or absent at the haematoma site on the right side of the brain. Using micro-PET/CT, ROIs were delineated to calculate the volume of brain haematoma in ICH mice model treated with or without W-POM NCs (Fig. 4I). PET and CT imaging analyses were performed to assess glucose uptake in haemorrhagic lesions in ICH mice model (Fig. 4J). The results showed that W-POM NCs treatment not only reduced the volume of the haematoma at 72 h after ICH but also improved glucose uptake by neural cells in the haematoma and perihematoma regions. Overall, these behavioural and imaging results confirmed that treatment with W-POM NCs rescued severely impaired behavioural and cognitive functions in ICH mice and alleviated direct damage caused by haematoma formation.

Multiangle therapeutic efficacy of W-POM in ICH mice model

Ferroptosis, a form of iron-dependent cell death centred on lipid peroxidation, plays an indispensable role in the pathology of ICH [39, 40]. MDA is a by-product of lipid peroxidation and can be an indicator of the extent of lipid peroxidation and oxidative stress within cells [41]. First, we measured the MDA levels in the perihematoma tissue. As shown in Additional file 4, the MDA content was significantly lower in the W-POM NCs-treated group than in the ICH group.

Iron regulatory proteins, such as transferrin receptor 1 (TFR1), divalent metal transporter 1 (DMT1), and ferroportin (FPN), regulate iron storage and transport when iron ion levels are elevated [42]. However, these regulatory mechanisms may fail, leading to an excessive accumulation of iron ions and ferroptosis. Therefore, WB was used to determine the expression of iron metabolism-related proteins (TFR1, DMT1, and FPN). According to the results and the quantitative analysis via WB (Fig. 5A–D), FPN levels in the brain tissue surrounding the haematoma in ICH mice model increased significantly after W-POM NCs treatment, whereas TFR1 and DMT1 levels decreased significantly. The detection of iron content based on brain tissue homogenates further confirmed the deposition of iron in perihematoma tissue (Additional file 5A, B). These results indicate that W-POM NCs treatment effectively reduced brain iron deposition and improved abnormal iron metabolism after ICH. Additionally, TEM images showed prominent ferroptosis characteristics, including mitochondrial membrane rupture and reduced or even vanished mitochondrial cristae, in the perihematoma tissue of the mice in the ICH

group, whereas these features were notably alleviated in the W-POM NCs-treated group (Fig. 5E).

Having established that W-POM NCs treatment effectively reduces iron deposition and protects the mitochondria, consequently inhibiting ferroptosis, further exploration of the broader impact of W-POM NCs treatment on neuronal health and the inflammatory response, which are key factors in ferroptosis, is crucial. First, we investigated the impact of W-POM NCs on ICH-induced neuronal injury using Nissl and FJB staining. Nissl staining indicated significant neuronal injury in the perihematoma region at 72 h post-ICH, characterised by a marked reduction in the number of neurons, shrinkage of neuronal cell bodies, and a significant decrease in Nissl body synthesis (Fig. 5F, H). Compared to the ICH group, the W-POM group showed a notable increase in the number of neurons, indicating that W-POM NCs treatment could alleviate neuronal injury in perihematoma tissue following ICH. Simultaneously, we examined neuronal degeneration through FJB staining, which marks damaged or dead neurons. Compared to the W-POM group, the ICH group showed a significant increase in the number of damaged neurons, marked by bright green fluorescence, indicating that W-POM NCs treatment had a satisfactory effect in preventing neuronal degeneration (Fig. 5G, I). These findings suggest that W-POM NCs exert protective effects against ICH-induced neuronal damage.

Given that GFAP and ionised calcium-binding adapter molecule-1 (Iba-1) are markers of astrocytes and microglia, respectively, their expression was assessed using immunofluorescence staining. As shown in Fig. 5J and K, the expression of GFAP and Iba-1 was significantly increased in the perihematoma region in the mice in the ICH group than in the Sham group. After administration of W-POM NCs, the expression of Iba-1 was significantly reduced ($p < 0.05$), whereas the expression of GFAP was not significantly different ($p > 0.05$). Semi-quantitative analysis of GFAP and Iba-1 positive cells in the perihematoma region further confirmed these changes in expression levels (Fig. 5L, M), indicating a decrease in the number of microglia after W-POM NCs treatment. Additionally, we measured the levels of inflammatory mediators using ELISA to assess inflammation in the affected area. The results showed that W-POM NCs significantly reduced the TNF- α , IL-6, and IL-1 β levels after ICH (Additional file 6 A–C). In summary, W-POM NCs simultaneously triggered multiple anti-ferroptosis pathways to treat ICH.

Intrinsic therapeutic mechanisms of W-POM against ferroptosis

To further evaluate the role of W-POM NCs in activating endogenous anti-ferroptotic pathways to combat

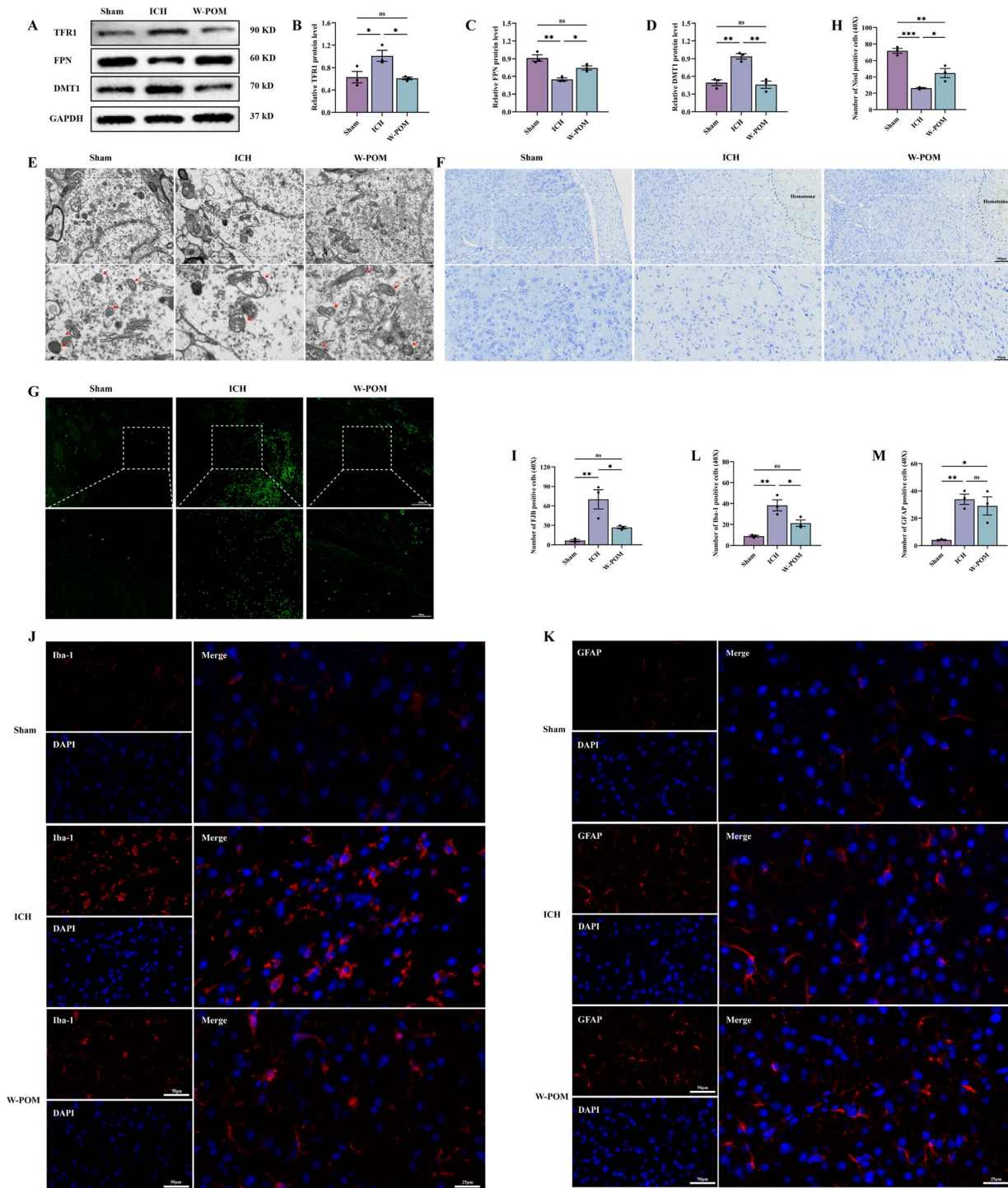


Fig. 5 W-POM NCs inhibit ICH-induced neuroinflammation, oxidative stress and ferroptosis in ICH mice model. **(a)** Protein expression of iron transport-related proteins (TFR1, FPN, DMT1) assessed using western blot. **(b-d)** Statistical graph of grayscale values of TFR1, FPN, DMT1 protein expression. **(e)** Representative TEM images of mitochondrial morphology of the neurons in the periaematoma area at 72 h after ICH. Red arrows indicate mitochondria. Representative images by Nissl staining **(f)** and FJB staining **(g)** in the periaematoma tissue showing the effects of W-POM NCs on ICH-induced neuronal injury and neurodegeneration. Statistical analysis of Nissl staining **(h)** and FJB staining **(i)** results in the periaematoma tissue. **(j)** Representative images of immunofluorescent staining for Iba-1 (red) and DAPI (blue) in the periaematoma area at 72 h after ICH. **(l)** Quantitative analyses of Iba-1 positive cells in the periaematoma area at 72 h after ICH. **(k)** Representative images of immunofluorescent staining for GFAP (red) and DAPI (blue) in the periaematoma area at 72 h after ICH. **(m)** Quantitative analyses of GFAP-positive cells in the periaematoma area at 72 h after ICH. (* $P < 0.05$, ** $P < 0.01$, *** $P < 0.001$, means \pm SEM). ICH, intracerebral haemorrhage; TEM, transmission electron microscopy; W-POM NCs, tungsten-based polyoxometalate nanoclusters; TFR1, transferrin receptor 1; DMT1, divalent metal transporter 1; FPN, ferroportin

ICH-induced secondary damage, proteomic analyses were conducted to identify potential targets and molecular regulatory mechanisms. We identified nine differentially expressed genes (DEGs), among which one gene was downregulated in the ICH group and upregulated in the W-POM group (Fig. 6A), whereas eight genes were upregulated in the ICH group and downregulated in the W-POM group (Fig. 6B). Gene Ontology (GO) enrichment analysis of the DEGs revealed the potential biological significance of gene functions, including biological processes (BP), cellular components (CC), and molecular functions (MF). The results indicated that these target genes were involved in BP, such as cell death, defence response, immune response, and inflammatory cell migration, as well as in MF and CC, such as antioxidant activity, TLR4 binding, arachidonic acid binding, long-chain fatty acid binding, and haemoglobin complex formation (Fig. 6C-E). Kyoto Encyclopedia of Genes and Genomes (KEGG) pathway analysis indicated that DEGs were involved in biological processes, such as the IL-17, peroxisome, and p53 signalling pathways (Additional file 7 A). These processes are directly linked to ferroptosis through the regulation of oxidative stress, lipid metabolism, and cellular responses to damage. Additionally, heatmap analysis showed that the sample distribution between the W-POM NCs-treated and ICH groups was clearly separated (Fig. 6F). After treatment with W-POM NCs, the expression of key genes that promote ferroptosis, such as S100A8 and S100A9, was significantly reduced.

Hub genes are central and highly connected genes within a gene regulatory network [43]. They play a critical role in maintaining the structure and function of biological networks. Hub genes were selected using the Cytoscape plug-in, Cytohubba. Six hub genes (S100A8, S100A9, Anxa1, Arg1, Lgals3, and Flrt3) were identified in the key module; their rankings and details are shown in Additional file 7B. These hub genes were then introduced into the STRING online database to construct a visual protein-protein interaction network (Additional file 7 C). Bioinformatics research has shown that ferroptosis is closely related to the therapeutic mechanism of W-POM NCs. W-POM NCs may exert therapeutic effects by inhibiting the expression of the top-ranked hub genes (S100A8 and S100A9) and regulating ferroptosis-related pathways, ultimately inhibiting ferroptosis.

S100A8/A9 functions as a damage-associated molecular pattern, which binds to receptors such as TLR4 and RAGE to activate downstream signalling pathways [44, 45]. Next, we hypothesised that W-POM NCs regulate the expression of the TLR4/hepcidin/FPN signalling pathway by modulating S100A8/A9 expression, thereby improving abnormal brain iron metabolism, inhibiting ferroptosis, and mitigating secondary brain injury

after ICH. To verify whether W-POM NCs regulate the aforementioned pathways through S100A8/A9 involvement in ferroptosis, we injected S100A8/A9 overexpressing AAV or control AAV into the right corpus striatum of C57BL/6 mice. Four weeks after virus injection, autofluorescence of AAV-encoded EGFP was detected in the right corpus striatum of the mice, confirming successful virus transfection (Additional file 8). Subsequently, we induced ICH in mice using collagenase IV and treated them with W-POM NCs following a previously established method. Further validation and examination using WB (Fig. 6G) determined whether W-POM NCs could regulate the TLR4/hepcidin/FPN signalling pathway involved in ferroptosis through S100A8/A9. The expression of S100A8/A9 proteins in the ICH+AAV-S100A8/A9 and ICH+POM+AAV-S100A8/A9 groups was significantly higher than that in the ICH+AAV-NC and ICH+POM+AAV-NC groups, demonstrating the effectiveness of S100A8/A9 (Fig. 6H). As expected, compared to the ICH+AAV-S100A8/A9 group, the W-POM NCs-treated group significantly reduced the expression of TLR4 (Fig. 6K) and hepcidin (Fig. 6I) proteins in the ICH+POM+AAV-S100A8/A9 group, significantly reducing the expression of FPN (Fig. 6J). Based on these findings, we believe that W-POM NCs can regulate the expression of multiple molecules involved in ferroptosis through S100A8/A9, thereby reducing brain iron deposition and neuronal ferroptosis and consequently improving neuronal damage in ICH.

In vivo distribution and biosafety of W-POM in C57BL/6J mice

The efficacy of nanomedicines is significantly influenced by their safety profiles. We demonstrated the limited cytotoxicity of W-POM NCs in HT22 cells. Next, we assessed the biological safety of W-POM NCs after intravenous injection into healthy male C57BL/6J mice. After 3 days of continuous administration, we performed a systematic evaluation of the major organs (heart, liver, spleen, lungs, and kidneys) and biochemical markers of the blood in healthy mice. Haematoxylin and eosin staining findings showed that the major organ sections of the W-POM NC-treated mice did not exhibit significant pathological features (Fig. 7A). Furthermore, compared to untreated ICH mice, no significant changes in serum albumin (ALB) (Fig. 7B), alanine aminotransferase (ALT) (Fig. 7C), aspartate aminotransferase (AST) (Fig. 7D), creatinine (CREA) (Fig. 7E), globulin (GLO) (Fig. 7F), total bilirubin (Tbil) (Fig. 7G), total protein (TP) (Fig. 7H), or uric acid (UA) (Fig. 7I) levels were observed in ICH model mice treated with 40 or 400 mg/kg W-POM NCs, indicating that the impact on liver and kidney function was negligible. These results indicated

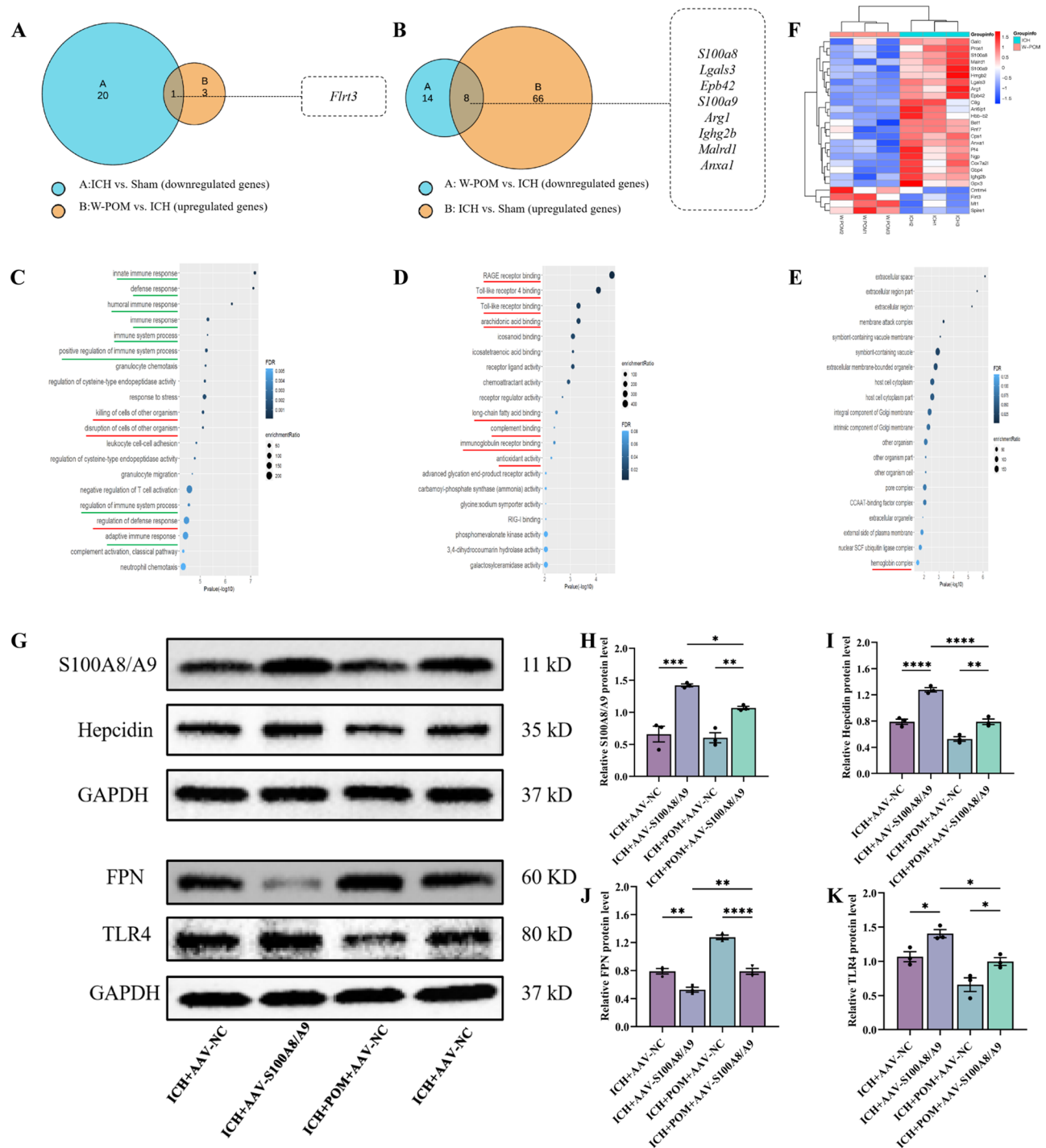


Fig. 6 Intrinsic defence mechanisms of W-POM NCs in inhibiting ICH-driven ferroptosis were investigated by proteomic analysis. **(a,b)** Venn diagram showing the intersection of target genes in ICH mice model and the sham group, with or without W-POM NCs treatment. **(c-e)** GO enrichment analysis of the identified DEGs, including the biological process, molecular function and the cellular component. **(f)** Heat maps of DEGs between the W-POM NCs-treated and ICH groups. Significantly downregulated proteins are marked in blue, whereas significantly upregulated proteins are marked in red. **(g)** Protein expression of S100A8/A9 and its downstream molecules after overexpressing S100A8/A9 in the right striatum area, assessed using western blot. **(h-k)** Statistical graph of grayscale values of S100A8/A9 and its downstream molecules protein expression after overexpressing S100A8/A9. * $P < 0.05$, ** $P < 0.01$, *** $P < 0.001$, means \pm SEM. DEGs, differentially expressed genes; ICH, intracerebral haemorrhage; GO, gene ontology; W-POM NCs, tungsten-based polyoxometalate nanoclusters

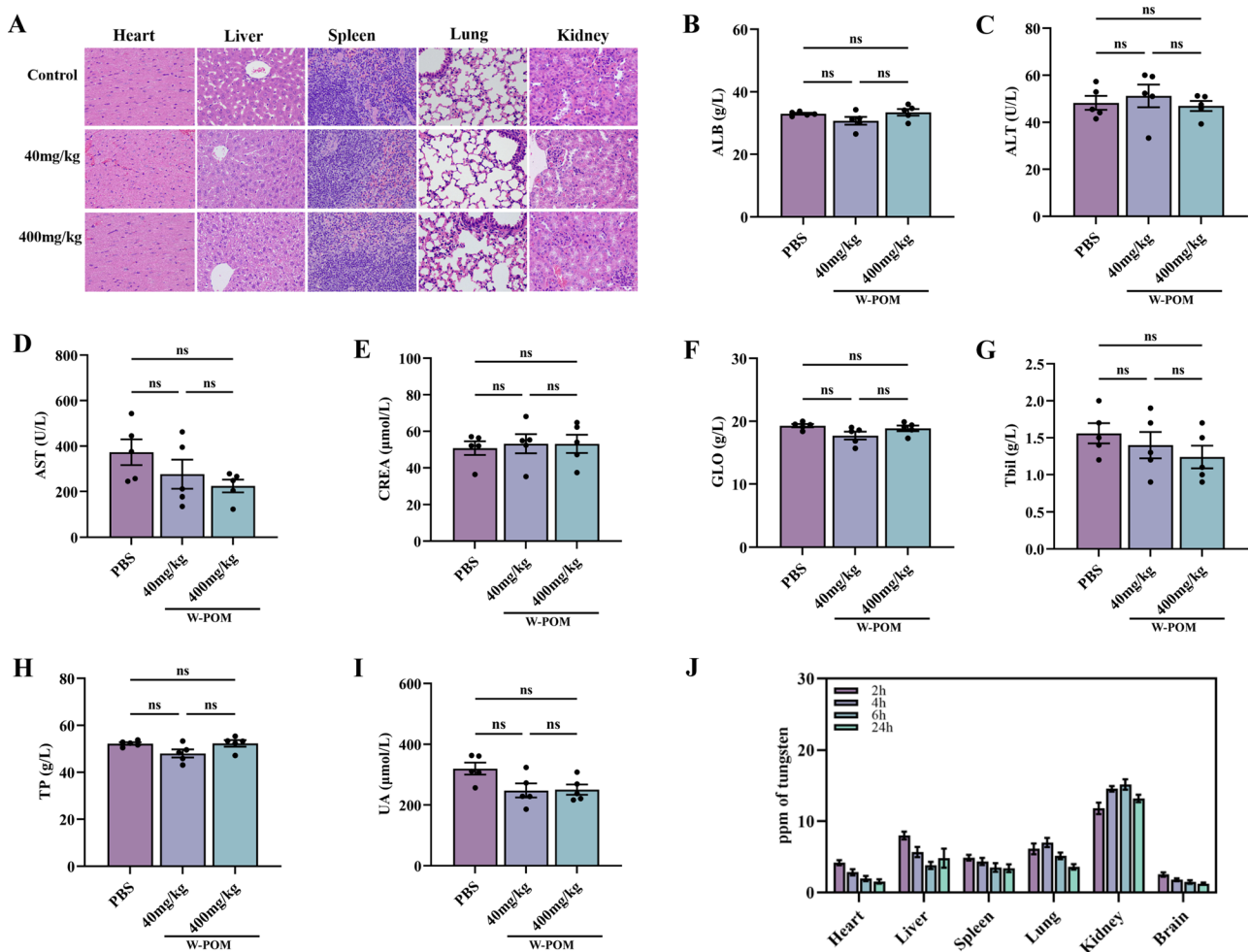


Fig. 7 Biosafety and biodistribution. **(a)** H&E staining images of major organs and **(b-g)** Blood biochemical test of healthy male C57BL/6J mice that received various treatments. **(h)** Biodistribution of W-POM NCs in major organs after intravenous injection in male C57BL/6J mice with W-POM NCs (40 mg/kg) at different time intervals. * $P < 0.05$, ** $P < 0.01$, *** $P < 0.001$, means \pm SEM. H&E, haematoxylin and eosin; W-POM NCs, tungsten-based polyoxometalate nanoclusters; ALB, albumin; ALT, alanine aminotransferase; AST, aspartate aminotransferase; CREA, creatinine; GLO, globulin; Tbil, total bilirubin; TP, total protein; UA, uric acid

the potential biocompatibility of W-POM NCs for future biomedical applications.

To analyse the biodistribution of W-POM NCs in the brain, we collected the main organs of ICH mice at different time points after administration of W-POM NCs and performed inductively coupled plasma-mass spectrometry (ICP-MS) analysis (Fig. 7j). The ICP-MS results indicated that the content of W-POM NCs in the brain remained stable throughout the experiment (1.77 ± 0.68 ppm). Interestingly, most of the W-POM NCs administered accumulated in the kidneys (13.69 ± 1.86 ppm). As a result of their small size, W-POM NCs were primarily excreted by the kidneys.

Discussion

ICH remains a major clinical challenge owing to the lack of effective treatments to directly reverse brain damage or reduce haematoma. Surgical interventions have

limited efficacy and are often associated with significant risks [46]. Despite advances in medical care, effective neuroprotective therapies for ICH are still lacking, highlighting the urgent need for novel therapeutic strategies.

Recent advances in nanomedicine have significantly enhanced the therapeutic strategies for ICH. The integration of nanomedicine into ICH treatment holds promise for enhancing therapeutic outcomes through improved drug delivery [47], effective antioxidative stress [48], anti-inflammatory [49], and other neuroprotective strategies. Continued research is necessary to achieve the full potential of these innovative approaches. Our study was the first to apply high-performance reduced W-POM NCs for the treatment of ICH, paving the way for new drugs, new approaches, and new mechanisms for ICH therapy. We demonstrated the efficacy of W-POM NC treatment, showing that it improved neurological deficits and motor impairments caused by ICH, and

provided neuroprotection from multiple perspectives. The mechanism may be achieved by regulation of ferroptosis through the S100A8/A9-mediated iron metabolism pathway.

Within the first 24 h after acute ICH, approximately 20% of patients experience haematoma expansion, which is closely associated with increased mortality and disability [50]. Additionally, haematoma expansion occurs predominantly within the first 6 h after the onset of ICH [51]. Therefore, early intervention to slow or prevent haematoma expansion could potentially serve as an effective therapeutic strategy. During the first 7 days after onset, brain oedema and inflammatory responses gradually develop, typically peaking on the Day 3 [52], which serves as a critical time point, often marking the peak of inflammation and brain oedema, and potential for further exacerbation of neurological deficits. Cao et al. [53] administered edaravone immediately after induction of ICH in rats and continued treatment for three consecutive days, demonstrating that edaravone alleviated sensorimotor deficits and neuronal pathological changes after ICH by reducing oxidative stress and mitochondrial damage. Gu et al. [54] also demonstrated that early intervention to suppress the immune response could mitigate neurological deficits after ICH, providing a promising neuroprotective strategy. Our study also demonstrated that early treatment with W-POM NCs led to a significant improvement in motor function in ICH mice, compared to those treated with saline. In addition to behavioural improvements, we also demonstrated the effects of W-POM NCs on haematoma development and cerebral metabolism. These results are crucial, as the formation of a haematoma after ICH creates mechanical pressure that directly damages the surrounding neural tissue. By reducing the size of the haematoma and improving metabolic activity, W-POM NCs likely reduce this direct damage and promote recovery. Above all, early intervention and monitoring during this stage are crucial to prevent worsening of the condition and to improve treatment outcomes.

Red blood cells rupture, releasing haemoglobin, which is further degraded to haeme and iron ions after ICH [55]. The accumulation of excess free iron ions generates a large amount of ROS through the Fenton reaction, triggering oxidative stress responses and catalysing lipid peroxidation [56]. The high mortality and disability rates associated with ICH are closely related to the irreversible death of neurons [57]. Previous studies had found that ferroptosis was crucial in the pathophysiology of ICH and is associated with dysregulated expression of various iron transport proteins [58, 59], such as FPN, TFR, and DMT1, induced by excessive iron deposition following ICH. TFR1 is a cell membrane receptor that binds to transferrin, an iron transporter protein in the blood

[60]. Elevated TFR1 levels increase iron import into cells, which can lead to an overload of intracellular iron. DMT1 is responsible for the transport of divalent metal ions, including ferrous iron (Fe²⁺), across cellular membranes [61]. Increased activity or expression of DMT1 can lead to higher intracellular iron levels. Similarly to TFR1, this can facilitate the accumulation of free iron, promoting ROS generation and lipid peroxidation, thus driving ferroptosis [62]. FPN is the only known iron exporter in mammalian cells, responsible for transporting iron from the inside of the cell to the extracellular space [63], and helps to maintain iron homeostasis by regulating iron efflux. Our study showed that ICH mice treated with W-POM NCs exhibited higher expression of FPN and lower expression of DMT1 and TFR1 proteins compared with ICH mice treated with saline. This indicated that W-POM NCs could promote the expression of iron export proteins and inhibit the expression of iron import proteins, thereby reducing intracellular iron deposition. At the same time, we demonstrated that the intervention of W-POM NCs reduced the total iron and ferrous iron content in iron-overloaded cell models and ICH mouse models. This suggested that W-POM NCs may reduce ICH-induced iron deposition by simultaneously regulating multiple iron transporters and modulating the multi-directional transport of iron ions.

Mitochondria are essential in ferroptosis, particularly since they serve as the primary sites for iron accumulation and ROS generation, which drive lipid peroxidation and result in ferroptosis [64]. ROS production promotes lipid peroxidation, particularly targeting polyunsaturated fatty acids in the mitochondrial membrane, resulting in membrane damage and loss of mitochondrial function [65]. Mitochondrial dysfunction further exacerbates oxidative stress, depletes ATP, and disrupts the mitochondrial membrane potential, ultimately driving the cell toward ferroptosis. Therefore, mitochondria act as initiators and amplifiers of the ferroptosis process [66]. Our study provided compelling evidence that W-POM NCs not only target mitochondria to reduce ROS levels but also restore mitochondrial function compromised by iron-induced oxidative stress. At the same time, neuronal degeneration and damage, along with neuroinflammation, are important factors in the ferroptosis process [67, 68]. These elements contribute to the deterioration of neuronal integrity and amplify the effects of oxidative stress, leading to cell death and exacerbating neuroinflammatory responses [69]. This relationship underscores the complexity of ferroptosis and its implications for ICH. In our study, W-POM NCs demonstrated a protective effect against ICH-induced neuronal injury, as evidenced by the preservation of normal neuron count and reduction of damaged neurons in the perihematoma region compared to saline intervention in ICH mice.

Furthermore, W-POM NCs effectively reduce microglial activation and lower inflammatory mediator levels, such as those of TNF- α , IL-6, and IL-1 β , in the periaematoma region of ICH mice, indicating their potential to activate multiple ferroptosis pathways for the treatment of ICH.

To further explore the anti-ferroptosis mechanism of W-POM NCs, we conducted proteomics analysis combined with bioinformatics analysis to identify drug targets. We found that among all DEGs, S100A8/A9 showed the strongest correlation with the regulation of secondary injury induced by iron overload after ICH. S100A8 (Calgranulin A) and S100A9 (Calgranulin B) are calcium-binding proteins that belong to the S100 protein family [70]. They typically form a non-covalent heterodimer known as calprotectin. This heterodimer (S100A8/A9) is biologically active and is more stable compared with individual monomers [71]. Their presence exacerbates brain injury by promoting infiltration and activation of immune cells, which release pro-inflammatory cytokines and chemokines, leading to secondary brain damage [72, 73]. However, they play a role in the regulation of oxidative stress by modulating ROS production [74]. S100A8/A9 can interact with TLR4, activating downstream signalling pathways [75]. Xiong et al. [76] had demonstrated that the TLR4/MyD88 signalling pathway can increase hepcidin levels in the brain and serum subsequent to ICH. The elevated hepcidin binds to FPN, thereby inhibiting iron export from the brain to the circulation following ICH. Hepcidin is a crucial iron regulatory protein that controls cellular iron export through the only known iron export channel, FPN, playing a significant role in iron metabolism regulation [77]. On Day 3 after ICH onset, the serum hepcidin levels of the patient reach a peak, which mirrors the inflammatory response trend following ICH [78]. Yang et al. [79] intervened using the AAV virus to overexpress hepcidin in the brains of ICH rats. They found that this significantly inhibited the ICH-induced increase in brain iron content and effectively improved behavioural and cognitive deficits in ICH rats. Hepcidin plays a complex role in ICH, and different studies have drawn varying conclusions about its effects on brain iron metabolism after ICH. Variations in experimental models, hepcidin expression levels, and the timing of interventions could lead to different outcomes. Therefore, it is necessary to further investigate the impact of W-POM NCs on hepcidin during the acute phase of ICH intervention. According to the above, targeting the inflammatory response not only helps reduce inflammatory damage but also alleviates the accumulation of brain iron caused by oxidative damage after ICH. Subsequently, we overexpressed S100A8/A9 in ICH mice using AAV to verify whether W-POM NCs regulate ferroptosis-related pathways through activation of S100A8/A9, and the

results aligned with our expectations. Therefore, based on the above the experimental results, we confirmed that W-POM NCs could regulate the expression of the TLR4/Hepcidin/FPN signalling pathway by modulating S100A8/A9, thereby improving abnormal brain iron metabolism, inhibiting ferroptosis, and mitigating secondary brain injury after ICH.

Safe nanomedicines are more likely to be administered at therapeutic doses without causing harm, thereby maximising their therapeutic potential. Ensuring biocompatibility minimises the risk of side effects and enhances the overall safety profile of the treatment, making it a viable option for clinical applications [80–82].

Our study also focused on the effects of W-POM NCs on vital organs. The results indicated that the W-POM NCs did not have an adverse impact on the functions of the heart, liver, spleen, lungs, and kidneys, suggesting that the intervention is relatively safe for the treatment of ICH. Furthermore, according to the ICP-MS results, we confirmed that W-POM NCs can effectively cross the BBB, which is essential for the drug to reach the site of the lesion and exert its therapeutic effects.

Our study has some limitations. While our findings suggested that W-POM NCs can effectively cross the BBB, the precise pathways through which W-POM NCs selectively target specific cell types, such as neurons, astrocytes, or microglia, remain unclear. Future studies could provide valuable insights into their intracellular trafficking and cell-specific effects. Exploring these aspects will deepen our understanding of their mechanism of action and enhance their therapeutic potential. Although we conducted bioinformatics analysis to identify S100A8/A9 as a key target gene, the functional significance of other DEGs in ICH still requires further *in vitro* and *in vivo* experimental investigation. Additionally, the long-term effects of these NCs on brain function and overall health require further investigation. Future studies should focus on the long-term safety profile of W-POM NCs and on their potential application in clinical settings. Furthermore, exploring the synergistic effects of W-POM NCs with other therapies may further enhance their therapeutic efficacy.

Conclusion

In this study, we successfully synthesised a NC using W-POM with high ROS scavenging efficiency, which showed excellent performance in alleviating ICH damage. W-POM NCs can modulate ferroptosis by improving abnormal brain iron metabolism and antioxidant activity, inhibiting neuronal damage, and reducing neuroinflammation. In particular, W-POM can effectively penetrate the BBB, significantly reduce brain oedema, and improve neurological function deficits in ICH mice. Our results further demonstrate that W-POM activates

the S100A8/A9-regulated TLR4/hepcidin/FPN signaling pathway, which is crucial to counteracting secondary damage induced by ferroptosis after ICH. In conclusion, the application of W-POM provides a promising therapeutic strategy for mitigating ICH damage, opening new prospects for nanomedicine-based interventions to improve ICH treatment.

Abbreviations

AAV	Adeno-associated virus
BBB	blood–brain barrier
CCK	Cell counting kit
CNS	Central nervous system
CT	Computed tomography
DCFH-DA	2',7'-dichlorofluorescein diacetate
DEGs	Differentially expressed genes
DMEM	Dulbecco's Modified Eagle Medium
DMT1	Divalent metal transporter 1
EDS	Energy dispersive spectroscopy
EGFP	Enhanced green fluorescent protein
ELISA	Enzyme-linked immunosorbent assay
ESR	Electron spin resonance
FAC	Ferric ammonium citrate
FDG	Fluorodeoxyglucose
FPN	Ferroportin
FTIR	Fourier transform infrared
GFAP	Glial fibrillary acidic protein
GO	Gene ontology
H&E	Haematoxylin and eosin
Iba-1	Calcium-binding adapter molecule-1
ICH	Intracerebral haemorrhage
ICP-MS	Inductively coupled plasma mass spectrometry
IL	Interleukin
MDA	Malondialdehyde
MMP	Mitochondrial membrane potential
MS	Mass spectrometry
NDS	Neurological disability score
OFT	Open field test
PBS	Phosphate-buffered saline
PET	Positron emission tomography
PFA	Paraformaldehyde
PI	Propidium iodide
POMs	Polyoxometalates
Pt ^{II} -PW ₁₁	Platinum-substituted polyoxometalate
ROIs	Regions of interest
SDS-PAGE	Sodium dodecyl sulphate-polyacrylamide gel electrophoresis
SUV	Standardised uptake value
TBST	Tris-buffered saline with 0.1% Tween-20
TEM	Transmission electron microscopy
TFR1	Transferrin receptor 1
TLR4	Toll-like receptor 4
TNF- α	Tumour necrosis factor- α
ROS	Reactive oxygen species
UV	Ultraviolet
WB	Western blotting
W-POM NCs	Tungsten-based polyoxometalate nanoclusters
XPS	X-ray photoelectron spectroscopy
XRD	X-ray diffraction

Supplementary Information

The online version contains supplementary material available at <https://doi.org/10.1186/s12951-025-03149-9>.

Supplementary Material 1

Acknowledgements

We sincerely appreciate the valuable feedback and insightful suggestions provided by our colleagues on the manuscript.

Author contributions

GJ, XT, HY and YY designed and supervised this study, YY, ML and RL conducted the majority of the experiments, and YY completed the manuscript. JY and PY analysed the data. ZS, DB and PZ participated in the experiments and data analysis. All authors read and approved the final manuscript.

Funding

This work was financially supported by the National Natural Science Foundation of China (52273304), the Sichuan Science and Technology Program (2022NSFSC0724, 2023NSFSC1575, 2023NSFSC0709), Young Elite Scientists Sponsorship Program by CAST (YESS) (2022-2024QNRC002), Central Nervous System Drug Key Laboratory of Sichuan Province (230011-01SZ), the Fundamental Research Funds for the Central Universities, Southwest Minzu University (ZYN2024006), the City-School Science and Technology Strategic Cooperation Project of Nanchong (22SXQT0365), Research and development project of Affiliated Hospital of North Sichuan Medical College (2023-22D004), and Youth project of North Sichuan Medical College (XJ2023008001).

Data availability

No datasets were generated or analysed during the current study.

Declarations

Ethical approval

All animal experiments were approved by the Welfare and Ethics Review Committee of Animal Experiments at the North Sichuan Medical College (Nanchong, China) [approval No. NSMC(A)2024(053)].

Consent for publication

Not applicable.

Competing interests

The authors declare no competing interests.

Author details

¹Affiliated Hospital of North Sichuan Medical College, 1 South Maoyuan Road, Nanchong, Sichuan 637000, China

²Institute of Neurological Diseases, North Sichuan Medical College, Nanchong, Sichuan, China

³Key Laboratory of General Chemistry of the National Ethnic Affairs Commission, School of Chemistry and Environment, Southwest Minzu University, Chengdu, Sichuan, China

Received: 7 October 2024 / Accepted: 22 January 2025

Published online: 19 February 2025

References

- Sheth KN. Spontaneous intracerebral hemorrhage. *N Engl J Med*. 2022;387(17):1589–96.
- Hilkens NA, Casolla B, Leung TW, de Leeuw F-E. Stroke. *Lancet*. 2024;403(10446):2820–36.
- Morris NA, Simard JM, Chaturvedi S. Surgical Management for primary intracerebral hemorrhage. *Neurology*. 2024;103(4):e209714.
- Seiffge DJ. Good treatment of Hyperacute Intracerebral Hemorrhage is as Easy as ABC. *Neurology*. 2024;103(2):e209614.
- Zille M, Farr TD, Keep RF, Römer C, Xi G, Boltze J. Novel targets, treatments, and advanced models for intracerebral haemorrhage. *EBioMedicine*. 2022;76:103880.
- Al-Kawaz MN, Hanley DF, Ziai W. Advances in therapeutic approaches for spontaneous intracerebral hemorrhage. *Neurotherapeutics*. 2020;17(4):1757–67.
- Zhu F, Zi L, Yang P, Wei Y, Zhong R, Wang Y, et al. Efficient Iron and ROS nanoscavengers for Brain Protection after Intracerebral Hemorrhage. *ACS Appl Mater Interfaces*. 2021;13(8):9729–38.
- Dodson M, Castro-Portuguez R, Zhang DD. NRF2 plays a critical role in mitigating lipid peroxidation and ferroptosis. *Redox Biol*. 2019;23:101107.
- Zhang X-D, Liu Z-Y, Wang M-S, Guo Y-X, Wang X-K, Luo K, et al. Mechanisms and regulations of ferroptosis. *Front Immunol*. 2023;14:1269451.

10. Chen X, Li J, Kang R, Klionsky DJ, Tang D. Ferroptosis: machinery and regulation. *Autophagy*. 2021;17(9):2054–81.
11. Kim J, Zhu Y, Chen S, Wang D, Zhang S, Xia J, et al. Anti-glioma effect of ginseng-derived exosomes-like nanoparticles by active blood-brain-barrier penetration and tumor microenvironment modulation. *J Nanobiotechnol*. 2023;21(1):253.
12. Patra JK, Das G, Fraceto LF, Campos EVR, Rodriguez-Torres MDP, Acosta-Torres LS, et al. Nano based drug delivery systems: recent developments and future prospects. *J Nanobiotechnol*. 2018;16(1):71.
13. Lv W, Liu Y, Li S, Lv L, Lu H, Xin H. Advances of nano drug delivery system for the theranostics of ischemic stroke. *J Nanobiotechnol*. 2022;20(1):248.
14. Sadowska-Bartosz I, Bartosz G. Redox nanoparticles: synthesis, properties and perspectives of use for treatment of neurodegenerative diseases. *J Nanobiotechnol*. 2018;16(1):87.
15. D'Agata F, Ruffinatti FA, Boschi S, Stura I, Rainero I, Abollino O et al. Magnetic nanoparticles in the Central Nervous System: targeting principles, applications and safety issues. *Molecules*. 2017;23(1).
16. Ma M, Liu Z, Zhao H, Zhang H, Ren J, Qu X. Polyoxometalates: metallodrug agents for combating amyloid aggregation. *Natl Sci Rev*. 2024;11(7):nwae226.
17. Lentink S, Salazar Marcano DE, Moussawi MA, Parac-Vogt TN. Exploiting interactions between polyoxometalates and proteins for applications in (Bio) chemistry and medicine. *Oxygen Chem Int Ed Engl*. 2023;62(31):e202303817.
18. Song N, Lu M, Liu J, Lin M, Shangguan P, Wang J, et al. A giant Heterometallic Polyoxometalate Nanocluster for enhanced brain-targeted glioma therapy. *Angew Chem Int Ed Engl*. 2024;63(10):e202319700.
19. Li S, Jiang D, Ehlerding EB, Rosenkrans ZT, Engle JW, Wang Y, et al. Intrathecal Administration of Nanoclusters for protecting neurons against oxidative stress in cerebral Ischemia/Reperfusion Injury. *ACS Nano*. 2019;13(11):13382–9.
20. Zhou H, Zhao C, Shao R, Xu Y, Zhao W. The functions and regulatory pathways of S100A8/A9 and its receptors in cancers. *Front Pharmacol*. 2023;14:1187741.
21. Habib A, Polavarapu R, Karmali V, Guo L, Van Dam R, Cheng Q, et al. Hepcidin-Ferroportin axis controls toll-like receptor 4 dependent macrophage inflammatory responses in human atherosclerotic plaques. *Atherosclerosis*. 2015;241(2):692–700.
22. Zhou J, Zhao W, Miao Z, Wang J, Ma Y, Wu H, et al. Folin-Ciocalteu assay inspired Polyoxometalate Nanoclusters as a renal Clearable Agent for Non-inflammatory Photothermal Cancer Therapy. *ACS Nano*. 2020;14(2):2126–36.
23. Yang R, Li J, Zhao L, Zhang M, Qin Y, Tong X, et al. Edaravone dextranolate regulates γ -aminobutyric acid transaminase in rats with acute intracerebral hemorrhage. *J Stroke Cerebrovasc Dis*. 2024;33(7):107738.
24. Clark W, Gunion-Rinker L, Lessov N, Hazel K. Citicoline treatment for experimental intracerebral hemorrhage in mice. *Stroke*. 1998;29(10):2136–40.
25. Gomes MJ, Neves Jd, Sarmento B. Nanoparticle-based drug delivery to improve the efficacy of antiviral therapy in the central nervous system. *Int J Nanomed*. 2014;9:1757–69.
26. Meng Q, Meng H, Pan Y, Liu J, Li J, Qi Y, et al. Influence of nanoparticle size on blood-brain barrier penetration and the accumulation of anti-seizure medicines in the brain. *J Mater Chem B*. 2022;10(2):271–81.
27. Yang F, Chen Y, Xiao Y, Jiang H, Jiang Z, Yang M, et al. pH-sensitive molybdenum (Mo)-based polyoxometalate nanoclusters have therapeutic efficacy in inflammatory bowel disease by counteracting ferroptosis. *Pharmacol Res*. 2023;188:106645.
28. Song D, Li C, Zhu M, Chi S, Liu Z. Tracking hepatic ischemia-reperfusion injury in Real Time with a reversible NIR-IIb fluorescent redox probe. *Angew Chem Int Ed Engl*. 2022;61(44):e202212721.
29. Zhao B, Ren Y, Zhang K, Dong Y, Wang K, Zhang N, et al. Hydroxypropyl methylcellulose reinforced bilayer hydrogel dressings containing L-arginine-modified polyoxometalate nanoclusters to promote healing of chronic diabetic wounds. *Carbohydr Polym*. 2024;342:122396.
30. Shen G, Zhou Z, Guo Y, Li L, Zeng J, Wang J, et al. Cholinergic signaling of muscarinic receptors directly involves in the neuroprotection of muscone by inducing Ca²⁺ antagonism and maintaining mitochondrial function. *J Ethnopharmacol*. 2024;319(Pt 2):117192.
31. Kessler A, Hedberg J, McCarrick S, Karlsson HL, Blomberg E, Odnevall I. Adsorption of horseradish peroxidase on metallic nanoparticles: effects on reactive Oxygen species Detection using 2',7'-Dichlorofluorescein Diacetate. *Chem Res Toxicol*. 2021;34(6):1481–95.
32. Li J, Jia Y-C, Ding Y-X, Bai J, Cao F, Li F. The crosstalk between ferroptosis and mitochondrial dynamic regulatory networks. *Int J Biol Sci*. 2023;19(9):2756–71.
33. Dong W, Gong F, Zhao Y, Bai H, Yang R. Ferroptosis and mitochondrial dysfunction in acute central nervous system injury. *Front Cell Neurosci*. 2023;17:1228968.
34. Gao M, Yi J, Zhu J, Minikes AM, Monian P, Thompson CB et al. Role of Mitochondria in Ferroptosis. *Mol Cell*. 2019;73(2).
35. Liu Y, Zhao D, Yang F, Ye C, Chen Z, Chen Y, et al. In situ self-assembled phytopolyphenol-coordinated Intelligent Nanotherapeutics for Multi-pronged Management of Ferroptosis-Driven Alzheimer's Disease. *ACS Nano*. 2024;18(11):7890–906.
36. Qiu S, Zhong X, Meng X, Li S, Qian X, Lu H, et al. Mitochondria-localized cGAS suppresses ferroptosis to promote cancer progression. *Cell Res*. 2023;33(4):299–311.
37. Fueger BJ, Czernin J, Hildebrandt I, Tran C, Halpern BS, Stout D et al. Impact of animal handling on the results of 18F-FDG PET studies in mice. *J Nucl Med*. 2006;47(6).
38. Deng L, Zhou L, Zhu Y, Fan G, Tang H, Zheng Y, et al. Electroacupuncture enhance therapeutic efficacy of mesenchymal stem cells transplantation in rats with Intracerebral Hemorrhage. *Stem Cell Rev Rep*. 2022;18(2):570–84.
39. Xie J, Lv H, Liu X, Xia Z, Li J, Hong E, et al. Nox4-and Tf/TfR-mediated peroxidation and iron overload exacerbate neuronal ferroptosis after intracerebral hemorrhage: involvement of EAAT3 dysfunction. *Free Radic Biol Med*. 2023;199:67–80.
40. Sun Y, Li Q, Guo H, He Q. Ferroptosis and Iron metabolism after Intracerebral Hemorrhage. *Cells*. 2022;12(1).
41. Wang Y, Quan F, Cao Q, Lin Y, Yue C, Bi R, et al. Quercetin alleviates acute kidney injury by inhibiting ferroptosis. *J Adv Res*. 2021;28:231–43.
42. Gong Y, Deng J, Wu Y, Xu X, Hou Z, Hao S, et al. Role of mass effect on neuronal iron deposition after intracerebral hemorrhage. *Exp Neurol*. 2023;368:114475.
43. Zhao P, Zhen H, Zhao H, Huang Y, Cao B. Identification of hub genes and potential molecular mechanisms related to radiotherapy sensitivity in rectal cancer based on multiple datasets. *J Transl Med*. 2023;21(1):176.
44. Du L, Chen Y, Shi J, Yu X, Zhou J, Wang X, et al. Inhibition of S100A8/A9 ameliorates renal interstitial fibrosis in diabetic nephropathy. *Metabolism*. 2023;144:155376.
45. Chen Y, Dong Y, Zhang Z-L, Han J, Chen F-S, Tong X-Y, et al. Fra-1 induces apoptosis and neuroinflammation by targeting S100A8 to modulate TLR4 pathways in spinal cord ischemia/reperfusion injury. *Brain Pathol*. 2023;33(1):e13113.
46. Kim JY, Bae H-J. Spontaneous intracerebral hemorrhage: management. *J Stroke*. 2017;19(1):28–39.
47. Reyes-Esteves S, Nong J, Glassman PM, Omo-Lamai S, Ohashi S, Myerson JW, et al. Targeted drug delivery to the brain endothelium dominates over passive delivery via vascular leak in experimental intracerebral hemorrhage. *J Control Release*. 2023;356:185–95.
48. Yang Y, Deng G, Wang P, Lv G, Mao R, Sun Y, et al. A selenium Nanocomposite protects the mouse brain from oxidative injury following intracerebral hemorrhage. *Int J Nanomed*. 2021;16:775–88.
49. Zi L, Zhou W, Xu J, Li J, Li N, Xu J, et al. Rosuvastatin Nanomicelles Target Neuroinflammation and improve neurological deficit in a mouse model of Intracerebral Hemorrhage. *Int J Nanomed*. 2021;16:2933–47.
50. Morotti A, Boulouis G, Dowlatshahi D, Li Q, Shamy M, Al-Shahi Salman R, et al. Intracerebral haemorrhage expansion: definitions, predictors, and prevention. *Lancet Neurol*. 2023;22(2):159–71.
51. Ovesen C, Christensen AF, Krieger DW, Rosenbaum S, Havsteen I, Christensen H. Time course of early postadmission hematoma expansion in spontaneous intracerebral hemorrhage. *Stroke*. 2014;45(4):994–9.
52. de Oliveira Manoel AL, Goffi A, Zampieri FG, Turkel-Parrella D, Duggal A, Marotta TR, et al. The critical care management of spontaneous intracranial hemorrhage: a contemporary review. *Crit Care*. 2016;20:272.
53. Cao S, Wei J, Cai Y, Xiong Z, Li J, Jiang Z, et al. Network Pharmacology Prediction and Experimental Verification for Anti-ferroptosis of Edaravone after Experimental Intracerebral Hemorrhage. *Mol Neurobiol*. 2023;60(7):3633–49.
54. Gu L, Chen H, Geng R, Sun M, Shi Q, Chen Y, et al. Single-cell and spatial Transcriptomics reveals ferroptosis as the most enriched programmed cell death process in Hemorrhage Stroke-induced oligodendrocyte-mediated White Matter Injury. *Int J Biol Sci*. 2024;20(10):3842–62.
55. Yang C, Han M, Li R, Zhou L, Zhang Y, Duan L, et al. Curcumin nanoparticles inhibiting ferroptosis for the enhanced treatment of Intracerebral Hemorrhage. *Int J Nanomed*. 2021;16:8049–65.

56. Wang Y, Wu S, Li Q, Sun H, Wang H. Pharmacological inhibition of Ferroptosis as a therapeutic target for neurodegenerative diseases and strokes. *Adv Sci (Weinh)*. 2023;10(24):e2300325.
57. Cao Y, Xiao W, Liu S, Zeng Y. Ferroptosis. Underlying mechanism and the crosstalk with other modes of neuronal death after intracerebral hemorrhage. *Front Cell Neurosci*. 2023;17:1080344.
58. Xiao Z, Shen D, Lan T, Wei C, Wu W, Sun Q, et al. Reduction of lactoferrin aggravates neuronal ferroptosis after intracerebral hemorrhagic stroke in hyperglycemic mice. *Redox Biol*. 2022;50:102256.
59. Lv B, Fu P, Wang M, Cui L, Bao L, Wang X, et al. DMT1 ubiquitination by Nedd4 protects against ferroptosis after intracerebral hemorrhage. *CNS Neurosci Ther*. 2024;30(4):e14685.
60. Wang D, Liang W, Huo D, Wang H, Wang Y, Cong C, et al. SPY1 inhibits neuronal ferroptosis in amyotrophic lateral sclerosis by reducing lipid peroxidation through regulation of GCH1 and TFR1. *Cell Death Differ*. 2023;30(2):369–82.
61. Tan Q, Zhang X, Li S, Liu W, Yan J, Wang S, et al. DMT1 differentially regulates mitochondrial complex activities to reduce glutathione loss and mitigate ferroptosis. *Free Radic Biol Med*. 2023;207:32–44.
62. Shi J, Yang MM, Yang S, Fan F, Zheng G, Miao Y, et al. MaiJiTong granule attenuates atherosclerosis by reducing ferroptosis via activating STAT6-mediated inhibition of DMT1 and SOCS1/p53 pathways in LDLR-/- mice. *Phytomedicine*. 2024;128:155489.
63. Bao W-D, Pang P, Zhou X-T, Hu F, Xiong W, Chen K, et al. Loss of ferroportin induces memory impairment by promoting ferroptosis in Alzheimer's disease. *Cell Death Differ*. 2021;28(5):1548–62.
64. Glover HL, Schreiner A, Dewson G, Tait SWG. Mitochondria and cell death. *Nat Cell Biol*. 2024;26(9):1434–46.
65. Zheng J, Conrad M. The metabolic underpinnings of Ferroptosis. *Cell Metab*. 2020;32(6):920–37.
66. Gan B. Mitochondrial regulation of ferroptosis. *J Cell Biol*. 2021;220(9).
67. Bao Z, Liu Y, Chen B, Miao Z, Tu Y, Li C, et al. Prokineticin-2 prevents neuronal cell deaths in a model of traumatic brain injury. *Nat Commun*. 2021;12(1):4220.
68. Cui Y, Zhang Z, Zhou X, Zhao Z, Zhao R, Xu X, et al. Microglia and macrophage exhibit attenuated inflammatory response and ferroptosis resistance after RSL3 stimulation via increasing Nrf2 expression. *J Neuroinflammation*. 2021;18(1):249.
69. Cui Y, Zhang Y, Zhao X, Shao L, Liu G, Sun C, et al. ACSL4 exacerbates ischemic stroke by promoting ferroptosis-induced brain injury and neuroinflammation. *Brain Behav Immun*. 2021;93:312–21.
70. Li Y, Chen B, Yang X, Zhang C, Jiao Y, Li P, et al. S100a8/a9 signaling causes mitochondrial dysfunction and Cardiomyocyte Death in response to Ischemic/Reperfusion Injury. *Circulation*. 2019;140(9):751–64.
71. Liao W-C, Chen C-T, Tsai Y-S, Wang X-Y, Chang Y-T, Wu M-S, et al. S100A8, S100A9 and S100A8/A9 heterodimer as novel cachexigenic factors for pancreatic cancer-induced cachexia. *BMC Cancer*. 2023;23(1):513.
72. He G-Y, Zhao C-H, Wu D-G, Cheng H, Sun L-A, Zhang D-L, et al. S100A8 promotes inflammation via toll-like receptor 4 after experimental traumatic brain injury. *Front Neurosci*. 2020;14:616559.
73. Wang Y, Shi Y, Shao Y, Lu X, Zhang H, Miao C. S100A8/A9hi neutrophils induce mitochondrial dysfunction and PANoptosis in endothelial cells via mitochondrial complex I deficiency during sepsis. *Cell Death Dis*. 2024;15(6):462.
74. Gomes LH, Raftery MJ, Yan WX, Goyette JD, Thomas PS, Geczy CL. S100A8 and S100A9-oxidant scavengers in inflammation. *Free Radic Biol Med*. 2013;58:170–86.
75. Hou C, Wang D, Zhao M, Ballar P, Zhang X, Mei Q, et al. MANF brakes TLR4 signaling by competitively binding S100A8 with S100A9 to regulate macrophage phenotypes in hepatic fibrosis. *Acta Pharm Sin B*. 2023;13(10):4234–52.
76. Xiong X-Y, Liu L, Wang F-X, Yang Y-R, Hao J-W, Wang P-F, et al. Toll-like receptor 4/MyD88-Mediated signaling of Hepcidin expression causing Brain Iron Accumulation, oxidative Injury, and cognitive impairment after Intracerebral Hemorrhage. *Circulation*. 2016;134(14):1025–38.
77. Bao X, Luo X, Bai X, Lv Y, Weng X, Zhang S, et al. Cigarette tar mediates macrophage ferroptosis in atherosclerosis through the hepcidin/FPN/SLC7A11 signaling pathway. *Free Radic Biol Med*. 2023;201:76–88.
78. Xiong X-Y, Chen J, Zhu W-Y, Zhao T, Zhong Q, Zhou K, et al. Serum hepcidin concentrations correlate with serum iron level and outcome in patients with intracerebral hemorrhage. *Neurol Sci*. 2015;36(10):1843–9.
79. Yang G, Qian C, Zhang C, Bao Y, Liu M-Y, Jiang F, et al. Hepcidin attenuates the iron-mediated secondary neuronal injury after intracerebral hemorrhage in rats. *Transl Res*. 2021;229:53–68.
80. Souto EB, Blanco-Llamero C, Krambeck K, Kiran NS, Yashaswini C, Postwala H et al. Regulatory insights into nanomedicine and gene vaccine innovation: Safety assessment, challenges, and regulatory perspectives. *Acta Biomater*. 2024;180:1–17.
81. De Jong WH, Borm PJA. Drug delivery and nanoparticles: applications and hazards. *Int J Nanomed*. 2008;3(2):133–49.
82. Nyström AM, Fadeel B. Safety assessment of nanomaterials: implications for nanomedicine. *J Control Release*. 2012;161(2):403–8.

Publisher's note

Springer Nature remains neutral with regard to jurisdictional claims in published maps and institutional affiliations.